Dynamics of Compact Vortex Rings Generated by Axial Swirls at Early Stage

Chuangxin HE[1, 2](何创新), Lian GAN[2*](干联) & Yingzheng LIU[1](刘应征)

[1] *Key Lab of Education Ministry for Power Machinery and Engineering*
School of Mechanical Engineering, Shanghai Jiao Tong University
Shanghai 200240, China

[2] *Department of Engineering, Durham University*
Durham DH1 3LE, UK

Manuscript revised in March 2020

[*] Corresponding author:
E-mail address: lian.gan@durham.ac.uk

Abstract

The present work concentrates on the study of flow dynamics of swirl vortex rings at the Reynolds number $Re = 20{,}000$ using a combination of the planar- and stereo-particle image velocimetry (PIV) measurements and dynamic delayed detached-eddy (dynamic DDES) simulation. Particular attention is paid to the identification of the large-scale azimuthal modes in the vortex ring propagation process. In the experiments, vortex rings are issued from piston-driven axial swirlers with the swirl number ranges from $S = 0$ to 1.10. The stroke ratio $L/D = 1.5$ is used to produce a compact vortex ring without trailing jet. PIV measurements are conducted in a water tank while the in-plane component flow velocities on the longitudinal center plane and the three-component flow velocities on the cross-section plane at several downstream locations according to the ring trajectories are obtained. In the simulation, the axial swirlers are also included while the piston motion is realized by imposing a time-dependent inflow condition. Two types of dynamic effects in the vortex ring propagation process are captured by the planar-PIV measurement. That are the arriving time effect and the azimuthal effect, which induces parallel shift of the vortex ring core and the radial tilting of the vortex sheet respectively. These modes are identified using the stereo-PIV results by applying the fast Fourier transfer (FFT) in the azimuthal direction, followed by the proper orthogonal decomposition(POD) on the radial and temporal direction. It shows that both $m = 0$ and 1 modes (m is the azimuthal wave number) coexist in the weakly swirled vortex rings, while the $m = 2$ mode arises and the $m = 0$ mode decays at high swirl numbers. The simulation also identifies the $m = 1$ and 2 modes while the $m = 2$ mode has large pitch with respect to the formation time.

Keywords: vortex rings, axial swirler, dynamics, azimuthal modes

1. Introduction

Turbulent pulsatile injection with swirl is potentially an effective way for flow momentum delivery and passive mixing control. This injection mechanism combines the well-investigated pulsatile (zero-swirl) injections like those in pulse combustion, and continuous swirling injection (swirling jets), and is thus expected to exhibit characteristics of both to some extent. Pulsatile injection involves the formation of a compact primary vortex ring with a coherent vortex core wrapped by a toroidal bubble propagating downstream according to its self-induced velocity or a starting jet with significant wake (trailing jet) left behind the primary ring bubble, depending on the stroke ratio of the injection. For swirling jets, flow structure breaks down more rapidly with the increasing swirl momentum and the flow is featured by self-excited azimuthal waves in a number of possible primary modes which induce the complex axisymmetric or helical motions.

Previous studies revealed the swirl effect on the dynamics of compact vortex rings having ideal (near) solid-body rotating swirl component in the flow at relatively low Reynolds number Re[1-3]. Such an ideal swirl profile, which is usually generated by a rotating injection nozzle in practice, is useful to study fundamental physics as it excludes a number of contaminating factors. However, it often is not applicable for industrial applications due to its implement difficulty, especially at high Re applications as they require an unfeasibly large rotation rate to maintain the same relative swirl strength. In these applications, for instance jet engines, swirl is usually generated by a stationary swirler installed near the exit of the injection nozzle. The fixed guiding vane geometry ensures the designed fixed ratio of axial and azimuthal momentum hence the relative swirl strength. However, compared to flow generated by solid-body rotation type of swirl, flow generated by axial swirlers exhibits significantly complicated secondary vortical structures and flow dynamics originated from the vanes, as demonstrated in our recent work[4]. It thus motivates this study to further investigate the interaction between the primary and secondary vortices and their role in the flow evolution, which is not yet well understood.

The present study focuses on the effects of swirl on compact turbulent vortex rings. According to Gharib et al.[5], the compactness of the vortex rings is characterized by the "formation number (F)" which represents the stroke ratio limit of the formation process. Previous studies on laminar vortex rings without swirl determined a formation number $F \lesssim 4$ for a broad range of flow conditions[5, 6], where a compact vortex ring forms without a wake behind it that cannot be entrained into the primary ring toroidal bubble. For swirling vortex rings at $Re = 20{,}000$, F was found linearly diminishing with increasing swirl number S[4]. At $S = 1.10$, F reduces to 1.8, significantly lower than the F limit found at $S = 0$. Physically this is because the increased swirl tends to flatten the Gaussian-like azimuthal vorticity distribution and changes the way the ambient fluids rolls-up to the vortex core. Comparing the flow generated by axial swirlers in experiments and the idealised solid-body rotation in large-eddy simulations (LES), this linear relationship is found to be insensitive to the detailed swirl velocity profile or the existence of the secondary vortices shed from the vane surface. However, the vorticity cancellation between the primary core vortices and the opposite signed vorticity induced by the swirl (augmented by the swirler hub and vanes) increased the circulation decay rate of the primary ring structure in further downstream regions. This resulted in very complex flow dynamics and thus the vortex ring behaviours deviated from the theoretical predictions worked for simple zero-swirl vortex rings[7].

In continuous swirling jets, the swirl-stabilization is achieved by the induction of a central recirculation zone near the nozzle exit when the swirling number S is large enough[8]; this effect is reflected as the enlargement of the radius in compact vortex rings due to the centrifugal effect[4]. Billant et al.[9] observed the vortex breakdown of their continuous jets when S reached a well-defined threshold, which was independent on Re or nozzle diameter. In addition, a number of researchers suggested the existence of self-excited axisymmetry and helical modes in swirling jets[10-13]. They played a dominant role in the flow dynamics before the vortex breakdown[14-16] and the scalar mixing[17]. According to Liang and Maxworthy[11], two critical swirl numbers, $S_{cr1} = 0.6$ and $S_{cr2} = 0.8$, exist based on which the dynamic feature of the swirling jet is remarkably different. For $S = 0$, Kelvin-Helmholtz (K-H) instability dominates the non-swirling jets with the formation

of vortex rings on the shear layer; for $0 < S < S_{cr1}$, these vortex rings become tilted but the spiral waves are merely secondary instabilities; for $S_{cr1} < S < S_{cr2}$, the helical mode with azimuthal wave number m = 2 or 3 co-exist but are less coherent; while for $S > S_{cr2}$, a strong wave is stabilised at m = 1 after the breakdown of the vortex ring. However, it is not known whether similar critical swirl numbers also exist that can characterize different regimes of the flow dynamics in compact swirling vortex rings.

The flow becomes highly complex when swirl is superimposed to compact vortex rings, as demonstrated in a limited number of studies. Naitoh et al.[3] generated their vortex rings at Re = 1,600 and 2,300 by injecting fluid from a rotating nozzle using a cylinder-piston devise. Different swirl numbers were achieved by adjusting the rotation rate of the nozzle and the maximum equivalent swirl number Eqn. (26) in their experiment was $S = 1.5$. They found that the amount of fluid discharged due to the so called 'peeling off' increases with S. The swirl in the vortex core attenuated the azimuthal deformation and thus the travelling distance of the vortex rings extended compared with the no-swirl cases. As Re increased by an order of magnitude, decreasing travel distances with increasing S was observed in both experiments and numerical studies[4]. Other scattered numerical studies[1, 2, 18] concentrated on the evolution of the three-dimensional vortex structures and the instability development mechanisms of the swirling vortex rings, where the swirl component was superimposed on the already formed ring with ideal Gaussian core. Although it was suggested that Gaussian initial conditions can produce swirling rings that were qualitatively similar to that produced by a piston[1], additional axial swirlers ineluctably complicate the flow field of high-Re turbulent vortex rings and induce dynamic features which have not be studied in detail in former studies.

Being the continuation of our previous work[4] on the formation process of turbulent swirling vortex rings, a combined experimental and numerical study focusing on the flow dynamics is systematically conducted. The three-dimensional structures of the vortex ring and evolution of the large-scale azimuthal model are presently investigated. The tested swirl number ranges from S =

0 to 1.10, which was previously quantified using the planar particle image velocimetry (PIV) across the nozzle exit plane. Stereo-PIV measurements are performed on the cross-section at specified downstream locations to obtain the two-dimensional three-components flow fields. To reveal the three-dimensional vortex ring characteristics and the fine structures, numerical simulations are performed using a dynamic delayed detached-eddy simulation (DDES) model[19]. The complex swirler geometries are included in the simulations to replicate the experiment conditions.

2. Experimental and Numerical Setups

The experiment is performed in a glass tank measuring 2,400 mm (length) × 900 mm (width) × 800 mm (depth) filled with tap water, as shown in Figure 1. The flow is supplied from a pipe which is mounted to the center of the end surface with an inner diameter $D = 40$ mm. The pipe extends into the tank for approximately 200 mm to eliminate wall effects on the flow. A piston driven by a stepper motor with a stroke-nozzle diameter ratio $L/D = 1.5$ is used to produce the compact vortex rings. This L/D ratio is lower than the smallest formation number F over the S range studied here, thus ensures structural compactness for all the S conditions according to our previous study[4]. The stepper motor drives the piston at the speed $U_0 = 500$ mm/s during the experiment with a constant acceleration and deceleration of 25 m/s^2, yielding a maximum Reynolds number $Re = 20{,}000$ based on D and U_0. The swirling component of the flow is generated by the 3D-printed 12-vane axial swirlers (see Ref[4] for details) whose swirling strength is governed by the vane trailing angle β at half-radius location. β is selected to be 0, 20, 30, 40, 50, 60 degree. The pros and cons of using the axial swirler to generate swirling vortex ring, comparing to other possible swirl generation mechanisms are discussed in Ref[4].

The flow fields in the streamwise $(x - y)$ plane are measured using planar PIV as shown in Figure 1(a). The global seeding of the complete tank is made using 10-μm silver coated hollow glass spheres (Dantec, Denmark). The illumination is realized by a 532-nm Nd:YAG Laser with sheet optics to produce a 1-mm-thick light sheets on the measurement plane. Two 12-bit CCD cameras with spatial resolution 1280×1024 pixels are used to capture the particle images at 4 image pairs per second synchronized with the laser exposure. The cameras are installed side-by-side to increase the field of view while maintaining a good spatial resolution. The time interval with each image pair is adjusted, yielding a maximum particle displacement of approximately 6 pixels, to decrease the measurement error. In total 100 fluid discharges (resulting in 100 independent realizations at each formation time tU_0/D) are performed for each S case and multiple measurements with different sample time shifts are also applied to 'artificially' increase the sample

rate. Particle images are processed by Davis 7.0 with sub-pixel accuracy (± 0.1 pixel according to the cross-correlation algorithm), and an interrogation window size of 16 × 16 pixels and 50% overlap, yielding a measurement grid of 1 mm × 1 mm approximately.

The three-component flow velocities on the cross-section ($y-z$) plane downstream of the nozzle exit is measured by stereo-PIV as shown in Figure 1(b). In total 6 downstream planes are measured: $X/D = 0.375$ (15mm), 0.625 (25mm), 1.125 (45mm), 1.375 (55mm), 1.875 (75mm) and 2.75 (110mm). Two prisms filled with tap water are glued onto both sides of the glass tank to reduce optical distortion effect from the water-air interface. Image sampling are synchronized at the instance when the vortex ring core is about to reach the measurement plane according to the ensemble averaged celerity of each S case[4]. The time interval between the neighboring piston motions in the present experiment is determined according to the dimensionless jet-off time parameter $\tau_{off} = U_{jet}t_{off}/d > 400$ to ensure sufficient separation between two fluid injections[20]; this jet-off time parameter is enlarged with increasing S and $\tau_{off} = 800$ is set for the highest tested swirl strength $S = 1.10$. For this set of measurement, a grooved dotted plate is used for the camera calibration. Davis 7.0 software is also used with the self-calibration procedure to reduce the measurement error induced by the misalignment between the laser sheet and the calibration plate. The interrogation window size used here is 32 × 32 pixels and overlay 50%, giving 1.5 mm × 1.5 mm vector grid spacing approximately. 100 realisations are sampled in each measurement plane and S case.

To better understand the fully three-dimensional flow structures, dynamic delayed detached-eddy simulation (dynamic DDES)[19] is performed incorporated with the axial swirler geometry. The computational domain is shown in Figure 2(a). The fluid is issued through the swirler of diameter D to a cylindrical domain of $16D$ in diameter and $22D$ in length. The nozzle geometries are identical to those used in the experiment. The nozzle exit extends into the computational domain by $2D$ to eliminate the wall effects. The unconstructed tetrahedral grid is used to discretize the swirler domain with 8 layers of prism grid for the boundary layer refinement as shown in Figure

2(b), resulting in approximately 4 million cells for the swirler body. For the large cylindrical domain, a structured O-type base grid with 0.6 million cells is used with a static local grid refinement scheme employed to increase the grid resolution around the vortex ring structure ($-1.5 < r/D < 1.5$ and the streamwise range according to the measured ring traveling distance). This is achieved by dividing each grid cell into eight smaller ones at each refinement level in the regions specified. This results in maximum 14 million cells in total with 400 nodes in the azimuthal direction using two levels of grid refinement (fine grids). Coarse grids are also considered for the grid-independence test using one level of grid refinement (200 nodes in the azimuthal direction). The two regions of different grid topologies are connected using the arbitrary mesh interface (AMI) for the information exchange during the computation.

Uniformly distributed inflow velocity is applied at the nozzle entrance, while the velocity profile and the turbulence fluctuation naturally develop inside the swirler. In addition, inflow acceleration and deceleration also match the piston motion in experiments. On the outflow boundary, the convective condition[21] is used to allow a natural flow out of the domain. The convective velocity is set as the instantaneous velocity in the previous iteration. The no-slip and free-slip boundary conditions are applied at the nozzle wall and far field respectively. The pressure is set to zero at the outflow plane and zero gradient at all other boundaries. The simulation is performed using the open-source code OpenFOAM (www.openfoam.org). To avoid the nonphysical fluctuations that result from the unbounded central differencing scheme in the simulation, the "filtered Linear" scheme is used to remove the high-frequency mode with staggering characteristics. The time step Δt is chosen to ensure that the maximum local CFL number is approximately 1.5.

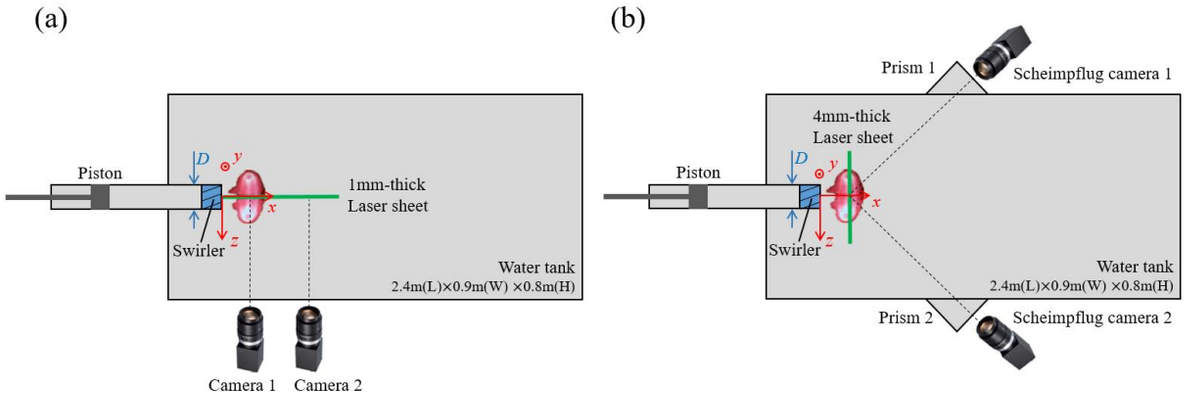

Figure 1 The schematic diagram (top view) of (a) the planar-PIV and (b) stereo-PIV measurements.

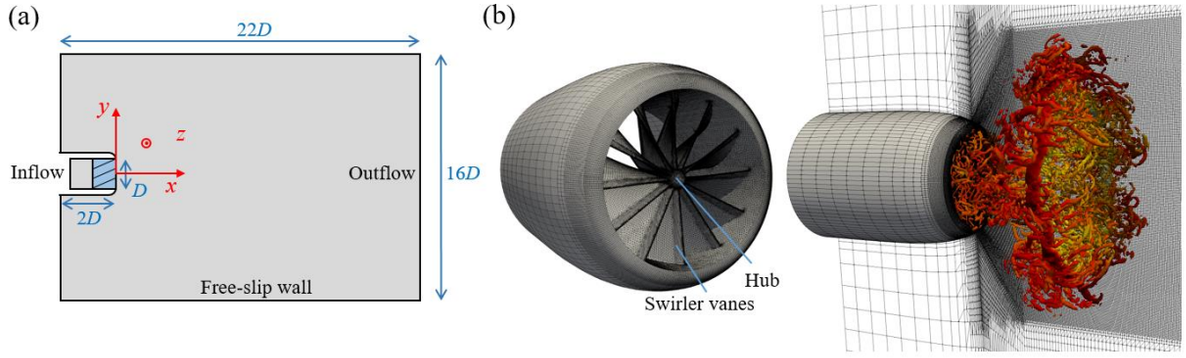

Figure 2 (a) The schematic diagram of the numerical setups (side view) and (b) the nozzle geometry with $\beta = 40^o$ and computational grid (isosuface shows the ring structure at $tU_0/D = 5$).

3. Dynamic DDES Formulation

Different from our previous work[4], the present simulation involves the vane surfaces inside the swirler which have considerable impacts on the velocity distribution. The dynamic DDES model[19] is used for the near-wall modeling of the flow inside the swirler to reduce the grid cells but retain comparable resolving of the small-scale vortical structures and their evolution out of the swirler with respect to LES. The formulation of the dynamic DDES model is reproduce here for clarification. The detailed description of this model is referred to our previous work[19]. The model is defined as

$$\frac{\partial k}{\partial t} + \nabla \cdot (\boldsymbol{U}k) = \nabla \cdot \left[\left(\upsilon + \frac{\upsilon_t}{\sigma_{k3}}\right)\nabla k\right] + P_k - \frac{k^{3/2}}{l_{des}}, \tag{1}$$

$$\frac{\partial \omega}{\partial t} + \nabla \cdot (\boldsymbol{U}\omega) = \nabla \cdot \left[\left(\upsilon + \frac{\upsilon_t}{\sigma_{\omega 3}}\right)\nabla \omega\right] + 2(1-F_1)\frac{\nabla k \cdot \nabla \omega}{\sigma_{\omega 2}\omega} + \alpha_3 \frac{\omega}{k} P_k - \beta_3 \omega^2, \tag{2}$$

and the eddy viscosity is determined by

$$\upsilon_t = L_{DES}\sqrt{k}\,. \tag{3}$$

Here, the two length scales l_{des} and L_{DES} are used, which are blended using the RANS and LES length scales,

$$l_{des} = f_d l_{les} + (1-f_d) l_{rans}\,, \tag{4}$$

$$L_{DES} = f_d L_{LES} + (1-f_d) L_{RANS}\,, \tag{5}$$

where

$$l_{les} = \frac{\Delta}{C_e}, \tag{6}$$

$$l_{rans} = \frac{\sqrt{k}}{C_\mu \omega}, \tag{7}$$

$$L_{LES} = C_k \Delta\,, \tag{8}$$

$$L_{RANS} = \frac{\alpha_1 \sqrt{k}}{\max(\alpha_1 \omega,\, F_2 S)}. \tag{9}$$

The definitions of the quantities and model constants follow the original $k-\omega$ SST model[22]. $\boldsymbol{U}$

is the Reynolds-averaged velocity vector in RANS mode or the filtered velocity vector in LES mode. f_d is the shielding function selecting RANS or LES modes in different regions. Δ denotes the grid length scale, which is also blended using the cubic root of the grid element volume V and the maximum grid length scale h_{max},

$$\Delta = f_d V^{1/3} + (1 - f_d) h_{max}. \tag{10}$$

The model coefficients C_k and C_e are dynamically computed as

$$C_k = \frac{1}{2}\frac{L_{ij} \cdot M_{ij}}{M_{ij} \cdot M_{ij}}, \tag{11}$$

$$C_e = \frac{(\upsilon + \upsilon_t)\left(\widehat{\|S\|^2} - \|\hat{S}\|^2\right)}{K^{3/2}/(2\Delta)}, \tag{12}$$

with

$$L_{ij} = \widehat{U_i U_j} - \hat{U}_i \hat{U}_j, \tag{13}$$

$$M_{ij} = -2\Delta\sqrt{k}\widehat{S_{ij}}, \tag{14}$$

$$K = \frac{1}{2}\left(\widehat{U_i U_i} - \hat{U}_i \hat{U}_i\right) \tag{15}$$

where "$\widehat{\ }$" denotes the filter operator at the test level.

The shielding function f_d is defined as

$$f_d = 1 - \max\{\tanh[(C_{d1} r_d \varphi_d)^{C_{d2}}], f_b\} \ (C_{d1} = 40, \ C_{d2} = 3). \tag{16}$$

with the following definition

$$\Gamma_u = \frac{\langle F_1 \sqrt{U_{ij} U_{ij}} \rangle}{\langle F_1 \rangle}, \tag{17}$$

$$\sqrt{\widetilde{U_{ij} U_{ij}}} = \Gamma_u \cdot \left(\frac{\sqrt{U_{ij} U_{ij}}}{\Gamma_u}\right)^{\sigma} \quad (\sigma = 0.9), \tag{18}$$

$$r_d = \frac{k/\omega + \upsilon}{\kappa^2 d_w^2 \sqrt{\widetilde{U_{ij} U_{ij}}}}, \tag{19}$$

Here, " $\langle\ \rangle$ " also represents the average in the whole computational domain. The damping function φ_d is determined from

$$\varphi_d = \left(\frac{\langle F_1 \cdot r^+ \rangle}{\langle F_1 \rangle}\right)^2, \tag{20}$$

where

$$\mathrm{y}^+_{local} = \max\left(\frac{h_{max}}{\eta h_{min}}, \frac{V^{1/3}\sqrt{U_{i,j}}}{\xi\sqrt{\upsilon}}\right) \qquad (\eta = 20, \xi = 5), \tag{21}$$

$$r^+ = \min[1, \max(\mathrm{y}^+_{local}, 1) - 1]\,. \tag{22}$$

The function f_b in Eqn. (16) is a limiter adopted from the IDDES model[23] to force a thin layer of RANS region near the wall when the local value of f_d decreases to zero. This thin layer is formulated within the viscous sublayer and thus has little effect on resolving the turbulence.

$$\alpha_1 = 0.25 - \frac{d_w}{h_{max}}, \tag{23}$$

$$f_b = \min\left[2e^{-9\alpha_1^2}, 1\right]. \tag{24}$$

4. Results and Discussion

4.1 Properties of swirling rings and validation

The swirl number S resulting from different swirler geometries were previously determined by measuring the axial/azimuthal velocity distribution in the nozzle exit plane at the steady state jet condition[4]. It is presented in Figure 3(a). S is defined as the ratio of the axial flux of the swirling momentum to that of the axial momentum[8],

$$S = 1.5\frac{\int_0^\infty U_0 U_\theta r^2 dr}{R\int_0^R U_0^2 r dr} \tag{25}$$

Here, the axial velocity approximates piston velocity U_0. U_θ is the azimuthal velocity measured by PIV at the nozzle exit. R is the nozzle radius and r is the radial coordinate defined by $\sqrt{y^2+z^2}$ with the origin set at the centre of the nozzle and on the nozzle exit plane. It is noted here ∞ is used as the upper limit of integration in the numerator to account for the flow radial entrainment. The coefficient 1.5 is employed to cast the S definition identical to that defined by Liang and Maxworthy[11] where the inflow fulfills solid-body rotation,

$$S = \Omega R/U_0 \tag{26}$$

where Ω denotes the flow angular.

The resultant S produced by the swirler ranges $0 \le S \le 1.10$, covering the two critical swirl numbers S_{cr} prevailing in swirling jet[11]. As the three-component velocity in $y-z$ plane have been obtained by stereo-PIV, instantaneous swirl number for the compact ring (S_{ring}) at different formation time can be calculated by Eqn. (25) and it is shown in Figure 3(b). Note S for each swirler is defined using the jet condition, i.e. $L/D \gg F$, whilst S_{ring} is for the ring generated by $L/D = 1.5 < F$. It is measured when the ring core is captured in the measurement plane according to the ring core trajectories (Figure 4), i.e. the maximum sectional swirl in the flow structure. It is clearly demonstrated that most of the measurements yield $S_{ring}/S > 1$ due to the entrainment

during the ring rollup. This has also been accounted for in Eqn. (25). However, larger S (larger β swirler) tends to give rise to smaller S_{ring}/S at fixed larger time. It is mainly attributed to the more rapid decay of the vortex rings caused by the higher turbulence level during the rollup process. In addition, Figure 3(b) shows a clear decay of S_{ring}/S with respect to the formation time. This decay rate shows a subtle increasing trend with S. An exception can be observed for $S \leq 0.41$ where S_{ring}/S remains almost constant for $tU_0/D < 8$, indicating a slow decay of swirl in weakly swirling rings during their early stage.

It is noted that as the measurement plane for each repeated realization is fixed, the resultant S_{ring} is subject to the uncertainty induced by the location perturbation of the ring core between different realizations at each specified formation time. Error bars for both S and S_{ring} are present in the figure, which are determined using 100 repeated flow realizations. With the above discussed uncertainty and turbulent condition of the vortex rings which yields significant difference between each flow snapshot, the swirl number calculated using different instantaneous fields exhibits notable variations. Thus all the discussions above are based on the data sample-averaged at the same formation time.

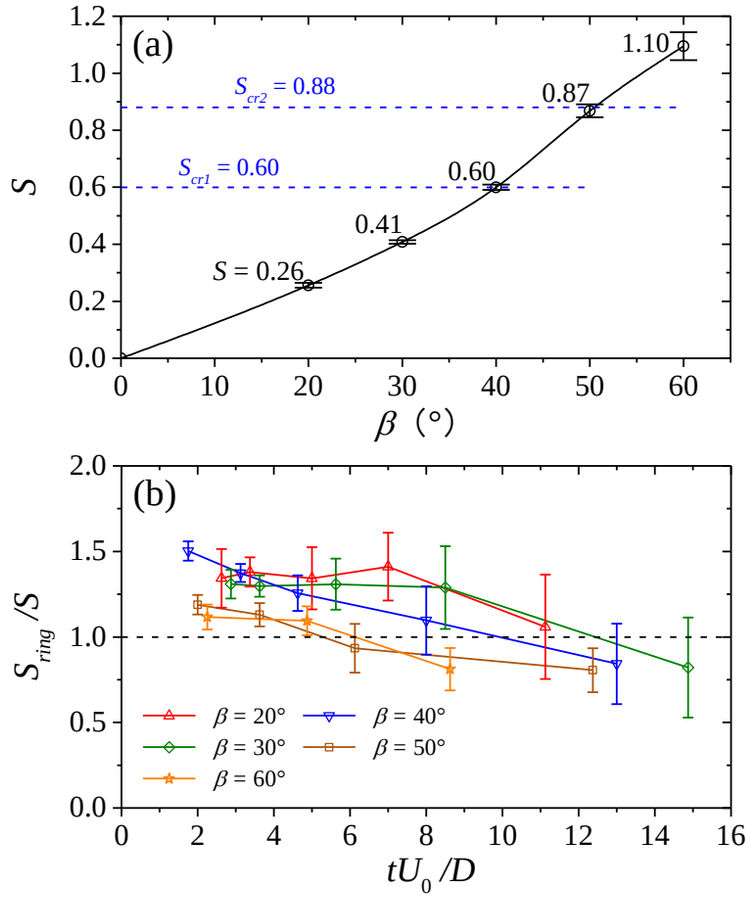

Figure 3 Fully developed swirl numbers of each swirler geometry measured by planar-PIV at the steady state jet condition (a) and the dependence of the maximum sectional swirl numbers of the flow on the formation time measured by stereo-PIV (b). Error bars are determined using 100 repeated flow realizations.

The dynamic DDES simulation is validated using the planar-PIV results. The axial trajectories of the vortex ring core are present in Figure 4, with both fine and coarse grids deployed for the grid-independent test. Since only one single discharge is simulated (multiple discharges are tested and they result in almost the same flow structure), the azimuthal averaging is performed to obtain the averaged core location. The fine grid returns the results agreeing reasonably well with the planar-PIV results[4] at $S > 0$. For $S = 0$ case, clear deviation occurs at $tU_0/D > 6$. The cause of this discrepancy is that the current grid resolution is not fine enough and thus yields a underestimation of the vorticity at the ring core at $x/D \geq 6$ and fails to capture the vortex evolution; this is further evidenced in Figure 5. While for $S > 0$ cases, the vorticity at the ring core

decays rapidly with time (evidenced in our previous work[4]), releasing the strict requirements on the grid resolution for the present simulation. The results obtained using the coarse grid show more discrepancy at large formation time for lower S cases. This strongly suggests the importance of sufficient grid resolution for small S cases in the simulation. To reassure the grid resolution effects on the simulation results, test is also performed by increasing the number of grid cells to approximately 25 million for $S = 0$ (results are not shown here). Although significant improvement of the result is observed, the axial trajectory of the ring core still deviates from the PIV results at larger formation time. According to Figure 4, therefore, simulation data at $tU_0/D > 6$ for $S = 0$ case is not employed for the later discussion, while the results at $tU_0/D < 6$ for $S = 0$ case and all those for other S cases based on the fine grid are included.

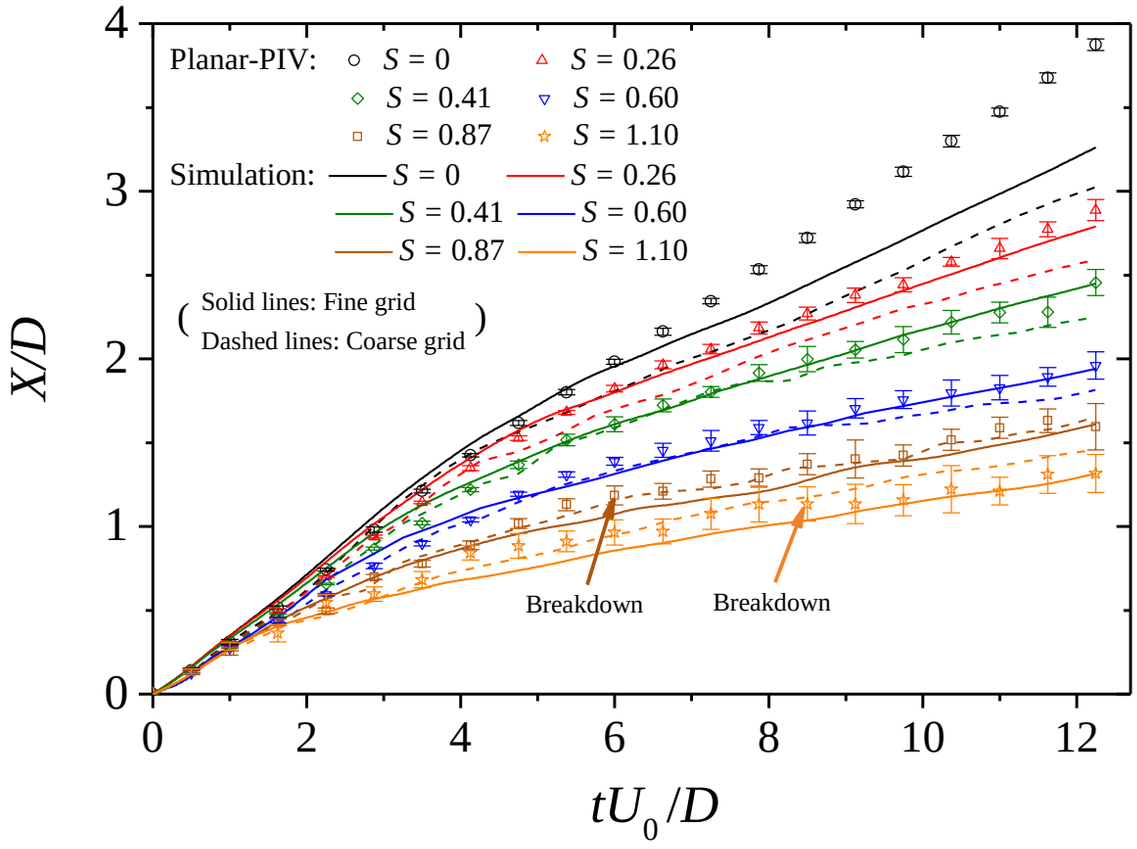

Figure 4 Axial trajectories of the vortex ring core: comparison of the present dynamic DDES results with the planar-PIV measurements. Error bars are determined using 20 repeated flow realizations.

(Fine grid: 2 levels of refinement; Coarse grid: 1 level of refinement)

The axial velocity distributions through the ring core obtained by the simulations and the planar-PIV measurements at $tU_0/D = 3$ and 6, are present in Figure 5. What needs to keep in mind here is that the simulation profiles are averaged in the azimuthal direction, but the PIV profiles are ensemble-averaged using 100 snapshots fixed at one azimuthal location (in the center of the gap between the two vane trailing edges). This contributes to the discrepancy between the two results at high S cases close to the nozzle exit where the non-uniformity of the flow is significant in the azimuthal direction. This can be observed for $S = 0.87$ and 1.10 at $tU_0/D = 3$, while a good agreement of the velocity distribution is obtained for $S \leq 0.6$ cases. After a considerable flow mixing at $tU_0/D = 6$, the simulation results agree better with the PIV measurements for all the cases except $S = 0$, reassuring the present simulation scheme. It is noted that for $S = 0$ case, the deviation is manifested by the attenuated velocity gradient in the simulation and the larger radius of the vortex ring. This is consistent with the results in Figure 4 where the discrepancy begins to occur at $tU_0/D = 6$. Our focus is on the $S > 0$ cases, where reasonable agreement is evidenced between the experiment and the simulation.

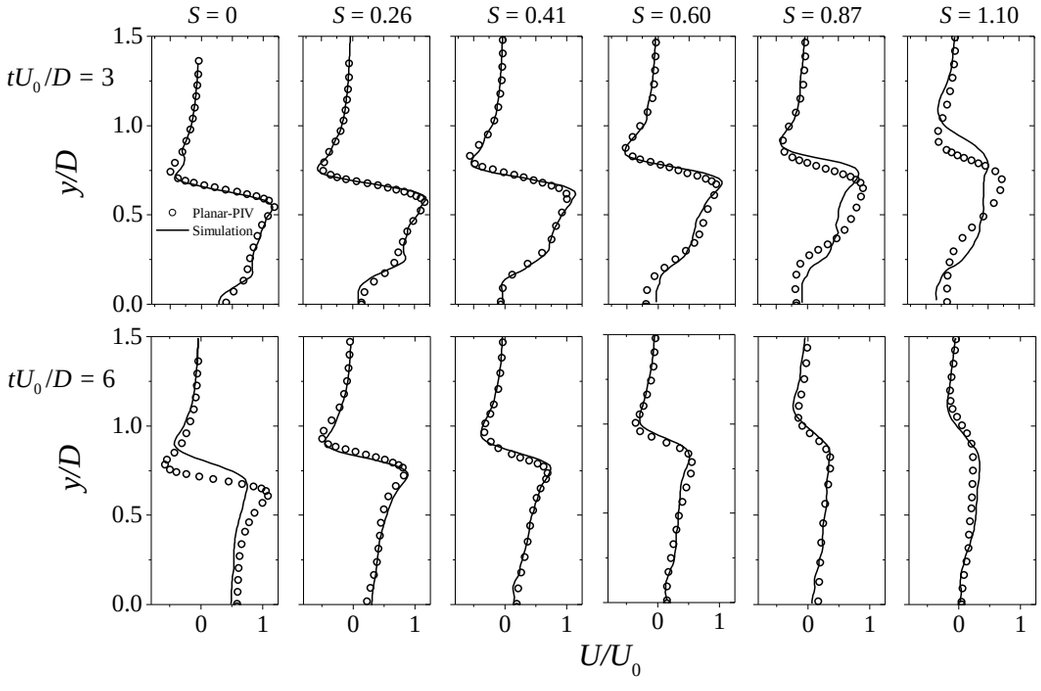

Figure 5 Comparison of axial velocity distributions of dynamic DDES and planar-PIV results at $tU_0/D = 3$ (upper row) and 6 (lower row).

Providing the accurate dynamic DDES simulation results, the transient swirl number behaviour over the formation time right at the swirler exit plane ($X/D = 0$) can be examined and it is shown in Figure 6. Here, the swirl number is normalized using the fully developed swirl number at the steady state condition, as presented in Figure 3(a). It is observed from Figure 6 that all the normalized swirl numbers almost overlap during the injection period, and stablise around 1 in the range of $0.4 < tU_0/D < 1.4$. This suggests that most of the fluid ejected by the stroke ratio $L/D = 1.5$ has been brought to swirl at the designed swirler number.

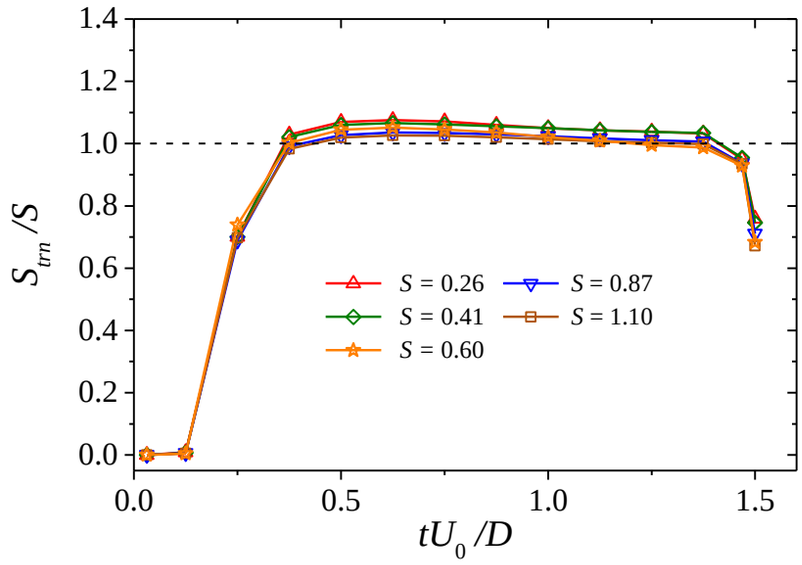

Figure 6 The transient swirl number at the swirler exit calculated using the simulation results.

4.2 Vortex structures and their evolution

The swirler vanes introduce secondary vortical structures to the flow field and they interact with the primary vortex ring core. Figure 7 illustrates the generation mechanism of the secondary vortices. The primary vortex ring is denoted by **A** in Figure 8. At the beginning of the discharge, the fluid in the region between two neighbouring vanes are accelerated whilst the fluid in the vane wake region downstream just starts to move from stationary by the viscous effect. This gives rise to two shear layers between the wake fluid (starting wake) and the fast moving fluid on both surfaces of a vane. In swirlers with $S > 0$, however, the fluid shear strain on the pressure side is higher than that on the suction side. This leads to the rollup of the vortex sheet in the radial direction, but tilted towards the pressure side behind each vane. It is denoted by **B** in Figure 8(b) ($tU_0/D = 0.38$). These starting wake vortices (**B**) form only at the very beginning of the flow discharge. At later time, the residual boundary layer vortex sheet (denoted by **C** in Figure 8) on the pressure side follows the starting wake vortices but cannot be rolled up into it. This is similar to the formation number effect in a starting jet (see Figure 8 (b)). Vorticity on the suction side is much weaker but does pronounce itself. The formation of these vortical structures (**C**) persist for the entire discharge duration and results in vortical structure of much higher vorticity magnitude compared with the wake type vortex at later time (see $tU_0/D \geq 0.50$ in Figure 8 (c-e)). Besides, another type of secondary vortex is the inner boundary vortices (**D**) upon the primary vortex ring, resulting from the rollup of the nozzle inner boundary layer and the corner between the inner wall and the vane surface. This can be observed having much smaller structures than that of the starting wake and vane boundary vortices at $tU_0/D = 0.38$, but growing rapidly , becoming stronger and interacting with the primary vortex ring. Figure 8 demonstrates the growing process of the vortex system for $S = 0.60$. The topological structures of the vortices are similar in different S cases, except for stronger secondary vortices at higher swirl numbers.

While the entire discharge process is set at L/D =1.5, which is smaller than the formation number (determining the primary vortex ring formation) for all the S cases, it can be further

divided into two stages in terms of secondary vortex initialization and growth: for $tU_0/D < 0.50$ all types of vortex structures start to form and undergo initial growth rather independently; for $tU_0/D > 0.50$ the formation of the starting wake vortices ceases while all the other type of vortices continue growing and start to interact with each other.

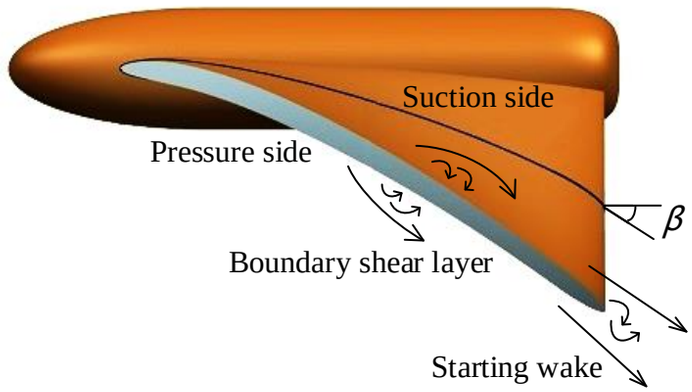

Figure 7 Schematic diagram of the starting wake and vane boundary vortices generation

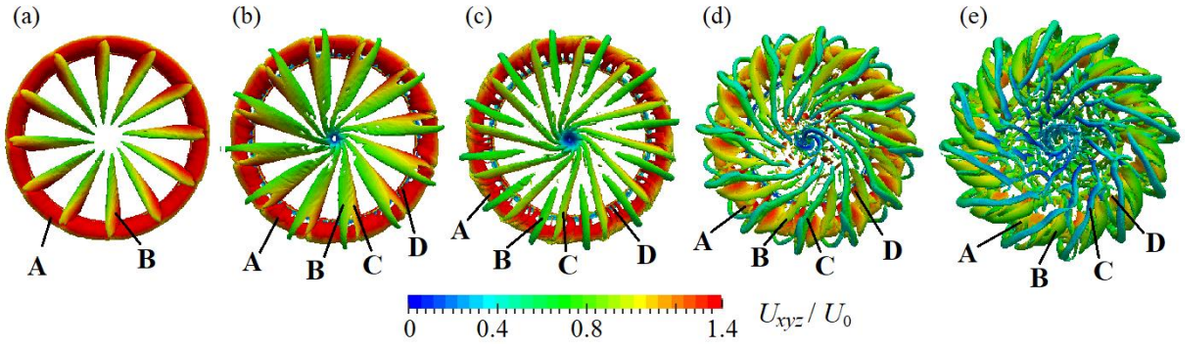

Figure 8 Three-dimensional structures of the primary vortex ring and secondary vortices for $S = 0.60$ at $tU_0/D =$ (a) 0.25, (b) 0.38, (c) 0.50, (d) 1.13 and (e) 1.50. Simulation results. $U_{xyz} = \sqrt{U_x^2 + U_y^2 + U_z^2}$ denotes the velocity amplitude in three-dimensional domain. Different vortical structures are named by: **A** primary vortex ring, **B** starting wake vortices, **C** vane boundary vortices and **D** inner boundary vortices.

It is believed that the complex vortex interaction promotes the breakdown of the vortex ring. Unlike in low Re cases, the breakdown process is difficult to define in the present high Re

complex structures, especially under the influence of secondary vortices. As visualized in Figure 9 and Figure 10, the breakdown can be seen through the combination of stereo-/planar-PIV measurements and simulation. The colormaps are adjusted separately in each subfigure so as to better visualize the vortical structures. For the $S = 0.26$ case in Figure 9, the primary ring structures are identifiable in both stereo- and planar-PIV measurements for $tU_0/D < 11.1$. The simulation reveals the three-dimensional structures and demonstrates the rapid decay of the secondary vortices and the longer survival of the primary vortex ring. When S is increased to 0.87, the breakdown process starts earlier at $tU_0/D = 6.1$ as shown in Figure 10. Breakdown here refers to the loss of the ring-like shape of the primary vortex in the simulation results. It is manifested by the loss of the core axisymmetry, or even a missing vortex core in vertical $(x - y)$ plane in PIV results. This is unlike the vortex breakdown in a continuous swirling jet at the same S, where a coherent helical (spiral) vortex is found established and attached to the nozzle exit[11]. In individual pulsatile flows produced by $L/D < F$, helical vortex cannot sustain individually. In other words, the vortex core will always tend to start as a ring shape regardless of the swirl strength. However, large-scale structure may start to emerge in forms of primary ring deformation with typical azimuthal wave numbers[18], or at larger time after the primary vortex core starts to break down under the effect of the secondary vortices and viscosity.

Breakdown of the vortex ring occurs even earlier for $S = 1.10$, which is evidenced in both PIV and simulation results (figures not shown). Generally speaking, stronger swirl leads to earlier breakdown of the primary vortex core. Two mechanisms are believed to contribute here. First, similar to a swirling jet[11], introducing swirl promotes the axial and azimuthal shear layer instability. This accelerates the development of the azimuthal wave along the vortex core and the instability of the wake shear layer behind the primary ring bubble. The highly unstable wake shear layer is then entrained and interact strongly with the primary vortex core. Second, the secondary vortices, whose intensity increases with S, are washed out from the vane surfaces. They are important feature of these swirler-generated vortex rings, which promote mixing and also contribute to rapid vortex breakdown.

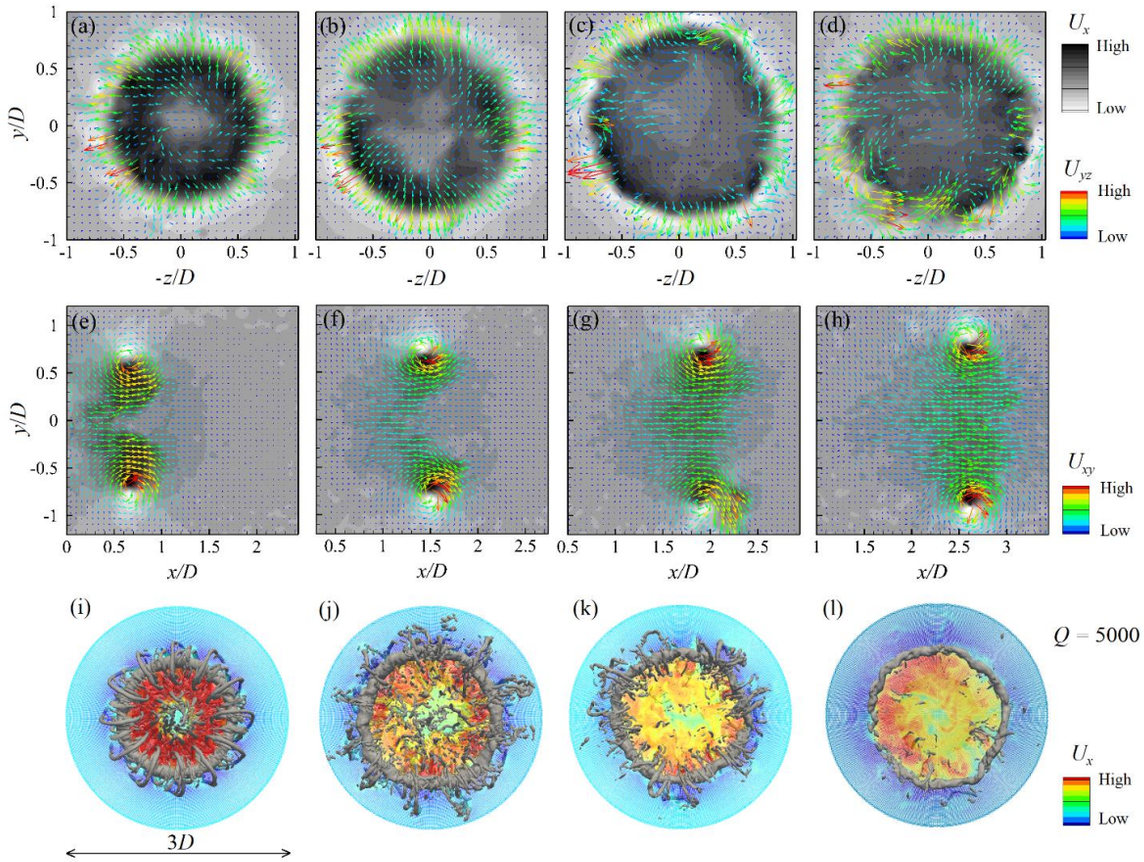

Figure 9 Instantaneous fields of the vortex ring of $S = 0.26$ at different formation time obtained by stereo-PIV (a~d), planar-PIV (e~h) and simulation (i~l). U_{xy} and U_{yz} denote the velocity amplitude in $x-y$ and $y-z$ planes.

(a) $tU_0/D = 2.6$, (b) $tU_0/D = 5.0$, (c) $tU_0/D = 7.0$, (d) $tU_0/D = 11.1$,
(e) $tU_0/D = 2.4$, (f) $tU_0/D = 4.9$, (g) $tU_0/D = 6.8$, (h) $tU_0/D = 11.1$,
(i) $tU_0/D = 2.6$, (j) $tU_0/D = 5.0$, (k) $tU_0/D = 7.0$, (l) $tU_0/D = 11.1$.

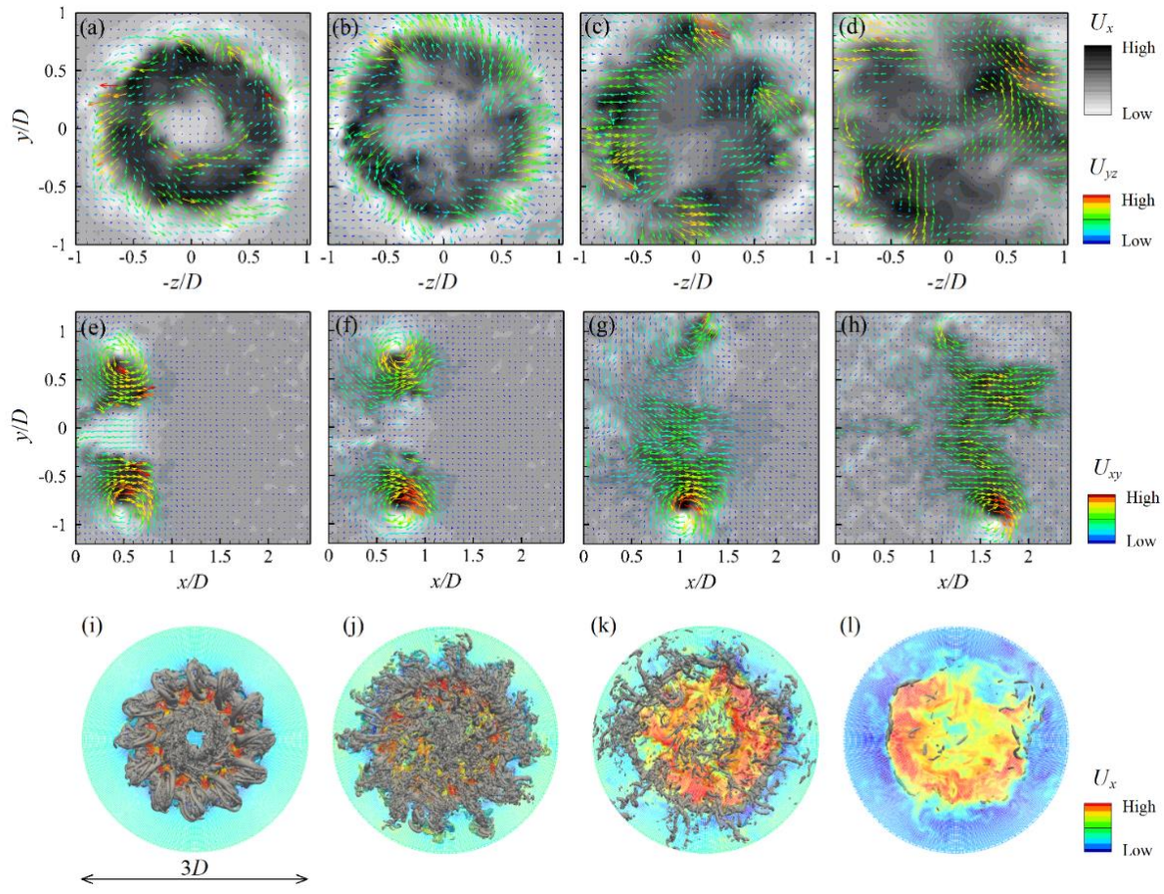

Figure 10 Instantaneous fields of the vortex ring of $S = 0.87$ at different formation time obtained by stereo-PIV (a~d), planar-PIV (e~h) and simulation (i~l). U_{xy} and U_{yz} denote the velocity amplitude in $x - y$ and $y - z$ planes.
(a) $tU_0/D = 2.0$, (b) $tU_0/D = 3.6$, (c) $tU_0/D = 6.1$, (d) $tU_0/D = 12.4$,
(e) $tU_0/D = 2.4$, (f) $tU_0/D = 3.6$, (g) $tU_0/D = 6.1$, (h) $tU_0/D = 12.4$,
(i) $tU_0/D = 2.0$, (j) $tU_0/D = 3.6$, (k) $tU_0/D = 6.1$, (l) $tU_0/D = 12.4$.

4.3 Large-scale azimuthal structures

The vortex rings observed in experiment undergo various organized azimuthal deformation before or even after the vortex breakdown. It is indicative by the existence of large-scale azimuthal modes during the ring evolution. Recalling the various axisymmetric and helical modes in the spatiotemporally varying fields of a swirling jet[11-13, 15, 16], similar signatures of these structures can also be detected in the present swirling vortex ring flows. By identifying the upper and lower vortex cores in the instantaneous planar-PIV data at different formation times, some motion characteristics can be visualized in Figure 11. The black dot represents each vortex ring core determined by the $|\omega|$ weighted centroid based on 50% threshold, and the flow field associated is presented by the vector fields. The green and orange dots denote the ring core locations of another two representative realizations at the same formation time. The scattering of the core locations can be inferred by two different types: the parallel shifted core location indicates the different arrival time of a ring bubble; the appeared tilted line suggests azimuthal waves of significant amplitude[7] (further evidenced in Figure 15 and Figure 16). The different arrival time, owing to the different average propagation celerity, can be attributed to the varying vortex core diameter and also manifested by the varying azimuthal wave amplitudes according to the Biot-Savart law. This is amplified by the swirl as it can be observed from the figure that in general the degree of the core location scattering at a given formation time increases with swirl number. However, it must be noted that to fully decouple the different arrival time effect and the wavy core effect would require volumetric measurements.

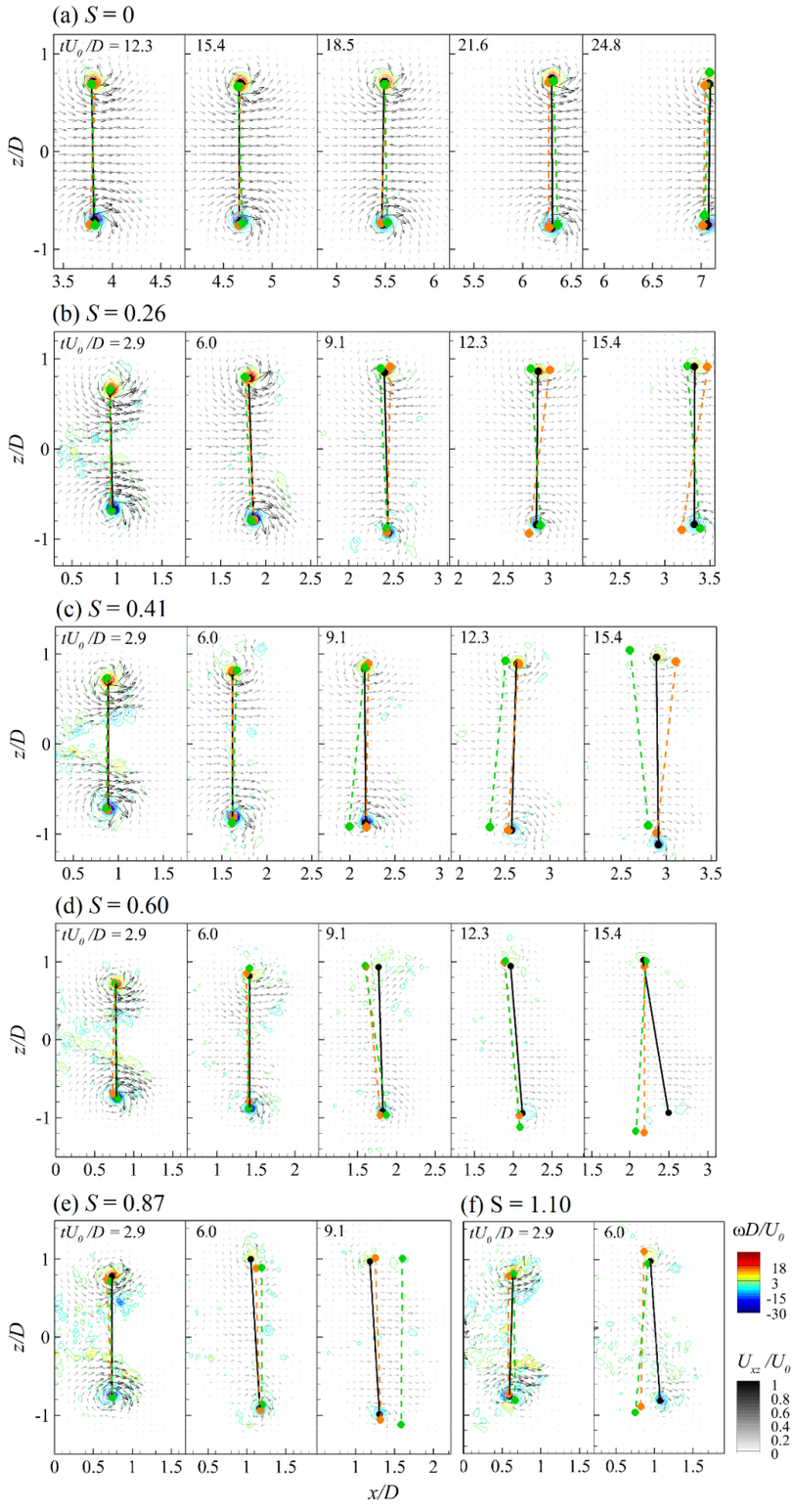

Figure 11 Instantaneous ring core location for three independent realizations (denoted by black, green and orange dots and bars) determined by planar-PIV. (a-f) for $S = 0$, 0.26, 0.41, 0.60, 0.87 and 1.10 respectively.

As an attempt to distinguish the ring core location scattering due to arrival time difference and the azimuthal waves, statistical analyses are performed using all the 100 samples. In Figure 12, X_{upper}, X_{lower}, Y_{upper} and Y_{lower} represent axial (X) and radial (Y) coordinates of the upper and lower vortex core centroid respectively determined using the planar-PIV results. "$\langle\ \rangle$" denotes the ensemble-averaged quantity. The abscissas $(\frac{X_{\mathrm{upper}}-\langle X_{\mathrm{upper}}\rangle}{\langle Y_{\mathrm{upper}}-Y_{\mathrm{lower}}\rangle})$ and ordinates $(\frac{X_{\mathrm{lower}}-\langle X_{\mathrm{lower}}\rangle}{\langle Y_{\mathrm{upper}}-Y_{\mathrm{lower}}\rangle})$ in Figure 12 denote the instantaneous shift of the location with respect to the averaged location, where $\langle Y_{\mathrm{upper}}-Y_{\mathrm{lower}}\rangle$ is the averaged ring diameter. In this plot, the clustered data points close to the solid line with 45-degree slope but away from the origin suggest the ring core location scattering due to arrival time difference as the distances of X_{upper} and X_{lower} to their means are in proportion, illustrated in (a) and (b). In contrast, the data points close to the dashed line with a negative slope tend to indicate vortex cores with wave developed; roughly. It must be stressed that these are based on statistical observations. Those data points near the 45-degree line may also have azimuthal waves developed along the core, broken down or not, but is not captured in the current measurement plane. Very clear arrival-time based core scattering prevails at large formation time for $S=0$ and 0.26 as shown in Figure 12(a). This is also illustrated at the last two formation times in Figure 11(a). However, this type of scattering is attenuated as S increases, taken over by the increased tendency of wave type of scattering (clustered roughly around the -45-degree slope line). It is noted that the data in Figure 12(c) are subject to influence of the complex flow dynamics of vortex ring, and thus a clear -45-degree inclination of the data points is difficult to obtain. large formation time are selected to emphasise the difference. The distribution of the data points at larger S (not shown) is similar compared with that at $S=0.41$ (Figure 12(c)).

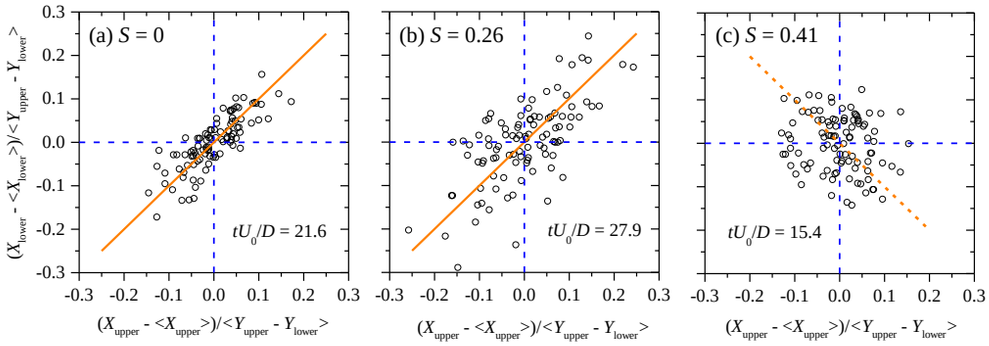

Figure 12 Coordinate maps of the upper and lower parts of the ring cores measured by planar-PIV. Each data point represents a realization. (a-c) for $S = 0$, 0.26 and 0.41 respectively.

To further investigate the development of the azimuthal wave along the vortex core reflected by the negative correlation as in Figure 12(c), the difference of the axial locations between the upper and lower vortex core in the ($x-y$) plane measurements, $\Delta X = \frac{X_{\mathrm{upper}}-X_{\mathrm{lower}}-\langle X_{\mathrm{upper}}-X_{\mathrm{lower}}\rangle}{\langle Y_{\mathrm{upper}}-Y_{\mathrm{lower}}\rangle}$ is calculated. Here, $\langle X_{\mathrm{upper}}-X_{\mathrm{lower}}\rangle$ is used to remove the effect of arrival time difference. For each realisation, ΔX is calculated at every formation time as shown by the gray lines in Figure 13(a), and finally the root-mean-square (rms) of ΔX value ΔX_{rms} is evaluated. Evidently, the magnitude of ΔX increases with time when azimuthal wave develops and its amplitude gets larger. This is also expected in vortex rings with zero swirl as azimuthal instability develops[24]. The comparison of ΔX_{rms} for different S cases clearly demonstrates its rapid increment with increasing S, implying the effect of swirl to promote faster azimuthal instability (waves) development. Close examination of Figure 13(b) seems to indicate a non-trivial jump of ΔX_{rms} from $S = 0.6$ to 0.87 at early time ($tU_0/D \approx 6$) and from $S = 0.26$ to 0.41 at larger time ($tU_0/D \gtrsim 12$). The former agrees with the two critical swirl numbers in a swirling jet[11]. Although for flow structures created by L/D =1.5, helical mode is less likely to form as mentioned earlier. It could imply a change of instability mechanism on the primary ring core. As at early time, it is significantly stronger than the secondary vorticies. The second jump could be more associated with the influence of the secondary vorticies as they have been interacting with the primary core for a period of time. For $S \geq 0.41$, it could be that the intensity of the secondary vorticies becomes similar. Note that for each S cases, ΔX_{rms} plot stops at the time after which the vortex core is

difficult to identify as the vortex structure is significantly broken or dissipated. It will be discussed further below.

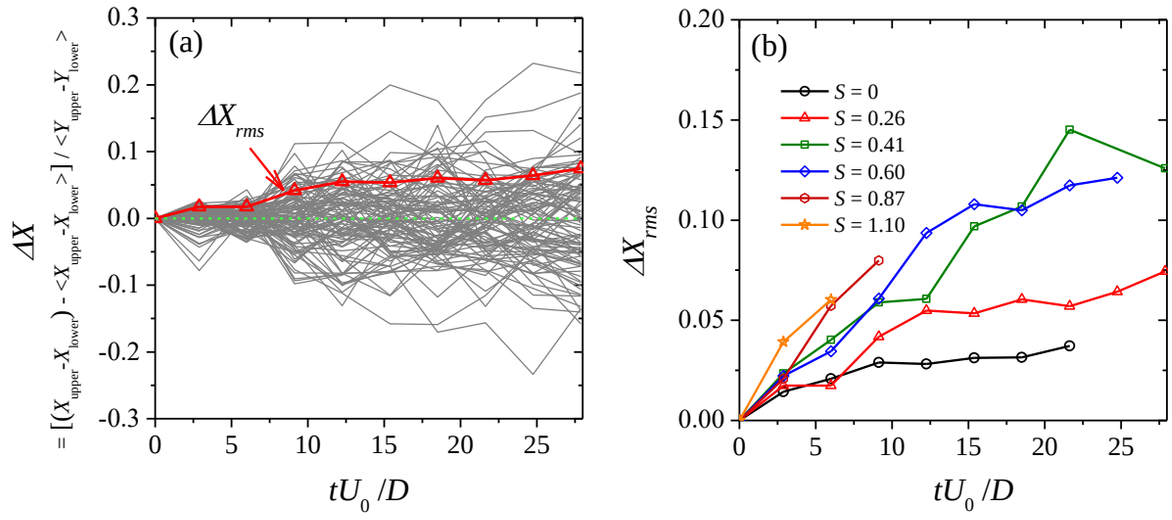

Figure 13 Variation of the axial distances between the upper and lower core measured by planar-PIV. 100 realizations and the corresponding root-mean-squares of $S = 0.26$ are plotted in (a), the variation of the root-mean-squares for different S is plotted in (b).

In order to better understand the possible coherent azimuthal wave structures in the flow, the Fast Fourier Transform (FFT) is performed in the azimuthal direction for the three-component velocity fields acquired by the stereo-PIV measurements. This maps the flow field from the physical domain $u'(r,\theta,t)$ to the azimuthal wavenumber domain $\hat{u}(r,m,t)$,

$$\hat{u}(r,m,t) = \int_0^{\infty} e^{-im\theta} u'(r,\theta,t) d\theta \tag{27}$$

where u' is the fluctuating part of the velocity field in which the mean field is subtracted. m is the azimuthal wavenumber, r, t and θ denote the radial, temporal and azimuthal coordinate respectively. The fluctuating velocity $u'(r,\theta,t)$ is converted from the Cartesian coordinates $u'(y,z,t)$ first and the realization number is used as the time. Thus each flow fluctuating field is decomposed to a linear combination of Fourier modes[25] with different azimuthal wave numbers. The normalized energy of each Fourier mode can be calculated as

$$E(m) = \frac{\int_0^T \int_0^\infty r[\hat{u}(r,m,t) \cdot \hat{u}(r,m,t)^*]\, drdt}{\sum_{m=0}^{\infty} \int_0^T \int_0^\infty r[\hat{u}(r,m,t) \cdot \hat{u}(r,m,t)^*]\, drdt} \tag{28}$$

"*" denotes the complex conjugate. $E(m)$ is a direct reflexing of the azimuthal mode proportion contained in the turbulent fluctuating flow fields.

For each streamwise location and S case, 100 realizations at the same formation time are used for FFT transform. Coordinate system is fixed for each case, while both the arriving time and the azimuthal wave effects are considered. Figure 14 presents the Fourier mode energy calculated at various measurement locations with different formation times. Only the Fourier modes with $m \leq 6$ are shown here due to the insignificant energy level at higher wavenumber modes. Since $E(m = 12)$, with m matching the vane number, is very low at the smallest formation time plotted ($tU_0/D \approx 2$) for all the S cases, it implies that the direct effect from the vanes is weak compared to the effect associated with the primary vortex structure. At larger time, owing to vortex interaction and viscous dissipation, it is expected that the vane effect becomes even weaker.

For the non-swirling vortex ring (with vanes) shown in Figure 14(a), the $m = 0$ mode dominates the flow for its early development $tU_0/D \leq 6.0$, as expected. The mode energy decays monotonously with the azimuthal wavenumber m. At $tU_0/D = 8.1$, however, the $m = 1$ mode emerges and becomes dominating the flow, whilst the $m = 0$ mode is slightly attenuated. This result is consistent with that observed in jet flows. It has been well understood that the (zero-swirl) round jet flows are dominated by large-scale helical ($m = 1$) and axisymmetric ($m = 0$) structures, which are referred to as the "preferred mode"[26]. Both the helical and the axisymmetric modes are present in the jet initial region, while the helical mode is the most dominant mode in the far field[27, 28].

In a linear stability analysis of swirling vortex rings at $Re_\Gamma = 10{,}000$[18], an analogy was made between the vortex ring and the Batchelor vortex pair, and the instability wave was decomposed to the out-of-plane ($x - y$ plane in the present study and axial direction for the Batchelor vortex pair)

and azimuthal (θ) directions. Several most rapidly amplified (unstable) out-of-plane modes were observed at each specified azimuthal wavenumber up to $m = 11$ for different S. However, the same identification process for the most dominant azimuthal modes may not be directly applied in the present highly non-linear turbulent flows, especially under the influence of the secondary vortices originated from the vanes. This is limited by the experimental technique used. The present work focuses on the determination of the dominant azimuthal wavenumber m in such complex highly turbulent swirling vortex rings.

Adding weak swirl to the vortex ring results in minor changes to the mode energy distribution in $S = 0.26$ cases as shown in Figure 14(b). Similar to the zero-swirl rings, it features the dominance of $E(m = 0)$ at small formation time $tU_0/D \leq 7$ overtaken by $E(m = 1)$ at larger formation time $tU_0/D = 10.6$. When the swirl number increases to $S = 0.41$ and 0.60, although the $m = 0$ and the $m = 1$ modes dominate the far field (large formation time), the $m = 2$ mode can be observed to take a transient lead as marked by Point 3 and Point 4 in Figure 14(c) and (d) respectively. This mode in both cases occurs at relatively small formation time, when the $m = 0$ mode is also suppressed, which is always the dominant mode at early time for smaller swirl number cases. Another significant observation is the decreasing of $E(m = 1)$ from $S = 0.26$ to 1.10 at the largest formation time measured (except $S = 0.4$ which is most probably due to the experimental uncertainty). This is contrasted by the growing of $E(m = 1)$, $E(m = 2)$ and $E(m = 3)$ over time in each $S > 0$ cases. In general, the proportion of the mode energy carried by the higher modes ($m > 6$) decreases as time. At large time, energy tends to be distributed on low m modes. This is highlighted by the comparable energy of the $m =$ 0, 1 and 2 modes at $S = 1.10$ case. Figure 14 demonstrates that, at weak swirl strength $S = 0.26$, the $m = 1$ mode has the highest energy at large formation time while the $m = 0$ mode dominates at earlier times. The $m = 2$ mode arises and is identifiable at moderate formation time for $S \geq 0.41$ while the $m = 1$ mode still dominates the ring dynamics at large formation time.

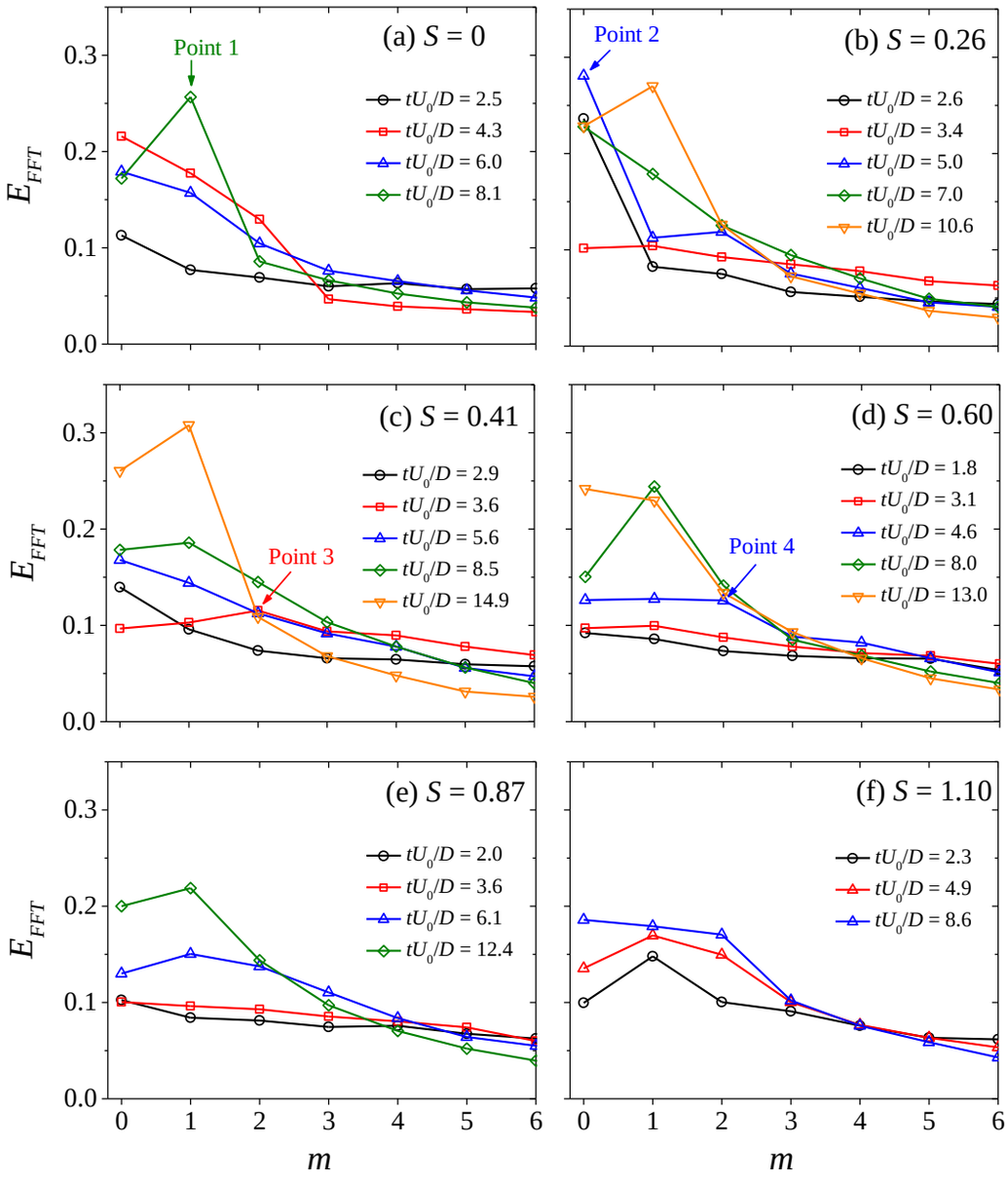

Figure 14 Energy of the Fourier modes at each azimuthal wavenumber calculated using stereo-PIV results. (a-f) for $S = 0$, 0.26, 0.41, 0.60, 0.87 and 1.10 respectively.

In order to extract the azimuthal modes with specified wavenumbers, the proper orthogonal decomposition (POD) is applied on the azimuthal spectral space of all the realizations in each case to identify the most energetic model shape, which is similar to the slice POD[29]. In the original slice POD, FFT is applied in both time and azimuthal directions to determine the frequency and wavenumber spectra; subsequently, the POD is applied only in the radial direction to extract the

large-scale structures at each specified frequency and azimuthal wavenumber. The slice POD method was successfully used to capture the preferred mode in jet flows[29, 30]. In the present study, since the PIV sample rate is not high enough to support FFT, the slice POD is modified so that FFT is only applied in the azimuthal direction, followed by POD in time and the radial direction. From this, the two-point cross-spectrum can be formulated as

$$A(r, r', m) = \langle \hat{u}(r, m, t)\hat{u}^*(r', m, t) \rangle \tag{29}$$

where "*" denotes the complex conjugate. The integral eigenvalue equation for the POD is then given by

$$\int B(r, r', m)\phi_i(r', m)dr' = \lambda_i(m)\phi_i(r, m) \tag{30}$$

where

$$B(r, r', m) = r^{1/2}A(r, r', m)r'^{1/2} \tag{31}$$

Hence, the final POD modes at each azimuthal wavenumber m are calculated as

$$\varphi_i(r, m) = r^{-1/2}\phi_i(r, m) \tag{32}$$

and the mode coefficients are determined by

$$a_i(m, t) = \int r^{1/2}\,\hat{u}(r, m, t)\phi_i^*(r, m)dr \tag{33}$$

After this process, the large-scale structures can possibly be extracted and visualized at each specified azimuthal wave number. The reconstruction using the first POD mode can usually capture the spatial pattern[29], viz the azimuthal modes in the present flow.

The spatial pattern of the azimuthal modes (the leading POD mode multiplied by the corresponding mode coefficient) at the selected points (Point 1 to 4 as shown in Figure 14 where their energy is distinct compared with other azimuthal modes at this formation time) together with the representative instantaneous fluctuating velocity at the corresponding time are shown in Figure 15. The mode pattern at other points with the same m appears similar. These azimuthal modes are the reduced order reconstruction for the large-scale pattern hidden in the fluctuating field. The lower modes, $m = 0$ and $m = 1$, reflect the flow features in the instantaneous fluctuating velocity field fairly well, as represented in Figure 15(a) and (b) for $S = 0$ and 0.26 respectively.

For higher modes, as $E(m)$ diminishes, their features are hard to visualise in the instantaneous fluctuating velocity. A distinctive feature of these higher modes is the clustering of higher energy structures, in the form of waves in the $x-$direction (reflected by the U_x fluctuation), close to the ring center, and these structures have a clear sense of rotation. These rotational waves also extend to the outer primary core and the bubble area in $S = 0.6$ cases. Whilst this properties also hold for larger S cases (figures are not shown), the mode shapes are more complex and difficult to identify in instantaneous fluctuation fields. Combining Figure 12, Figure 14 and Figure 15, it can be inferred that at larger time, the primary vortex core is responsible for the first two modes $m = 0$ and $m = 1$. The mode $m = 0$ is the arrival time effect and $m = 1$ mode is the effect of vortex core tilting. These two modes are also dominant in the classical zero-swirl vortex rings (see also Ref[7]). For smaller S cases, the core tilting seems to take the strongest effect, while the arrival time effect is more pronounced at large S cases. Also in weak swirl cases ($S \leq 0.41$) $m = 3$ mode is mainly retained in the central area of the bubble (as most energy is still carried by the core). As S increases, this mode and higher modes start to influence the core.

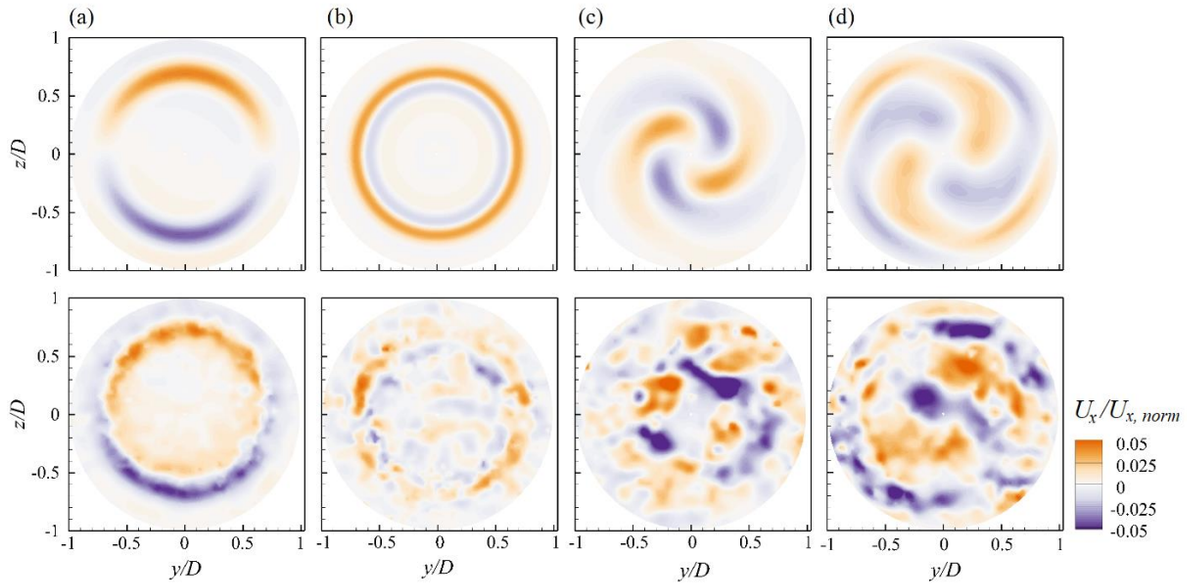

Figure 15 Azimuthal modes (upper) captured using stereo-PIV measurements and the instantaneous fluctuating axial velocity (lower) at the points marked in Figure 13. Point 1 (a), Point 2 (b), Point 3 (c) and Point 4 (d). velocity is normalized by the matrix norm $U_{x,norm}$.

These azimuthal modes can be better visualized in the simulation results. In Figure 16, the vortex rings visualized by the Q-criteria at $S = 0.26$ and 0.60 are selected for demonstration. According to the axial coordinate on each ring, the azimuthal modes $m = 1$ and 2 can be identified respectively. It shows that the primary ring-shaped core basically retains from formation to larger time. The azimuthal wave develops as time and the growth rate is roughly proportional to the swirl strength. Also as S increases, the influence from the secondary vortices becomes stronger and with their intensity comparable to the primary vortex core. These results reassure the existence of large-scale azimuthal modes in swirling vortex rings. The vortices shed from the vane surface remain subordinate during the entire range of investigation, i.e. they never dominate over the primary (wavy) vortex core. This agrees with the Fourier mode that $E(m = 12)$ stays insignificant over the entire investigation. The $m = 12$ mode is induced by the swirler vanes close to the swirler and rapidly decays during the formation time. The vanes influence the azimuthal structures of vortex ring indirectly by modifying its mean flow field and the generation of the vane trailing-edge vortices which interact with the primary vortex ring. It can be observed by the comparison of the azimuthal mode evolution in these two vortex rings that, the spiral pitch of the $m = 2$ mode at $S = 0.60$ (Figure 16(b)) is much larger than that of the $m = 1$ mode at $S = 0.26$ (Figure 16(a)). This can also be inferred from the round jet[30] in which the $m = 2$ mode evolves with lower frequency than that of the $m = 1$ mode, assuming that the vortex rings have similar dynamic features and the swirling effects on the mode evolution frequency is finite.

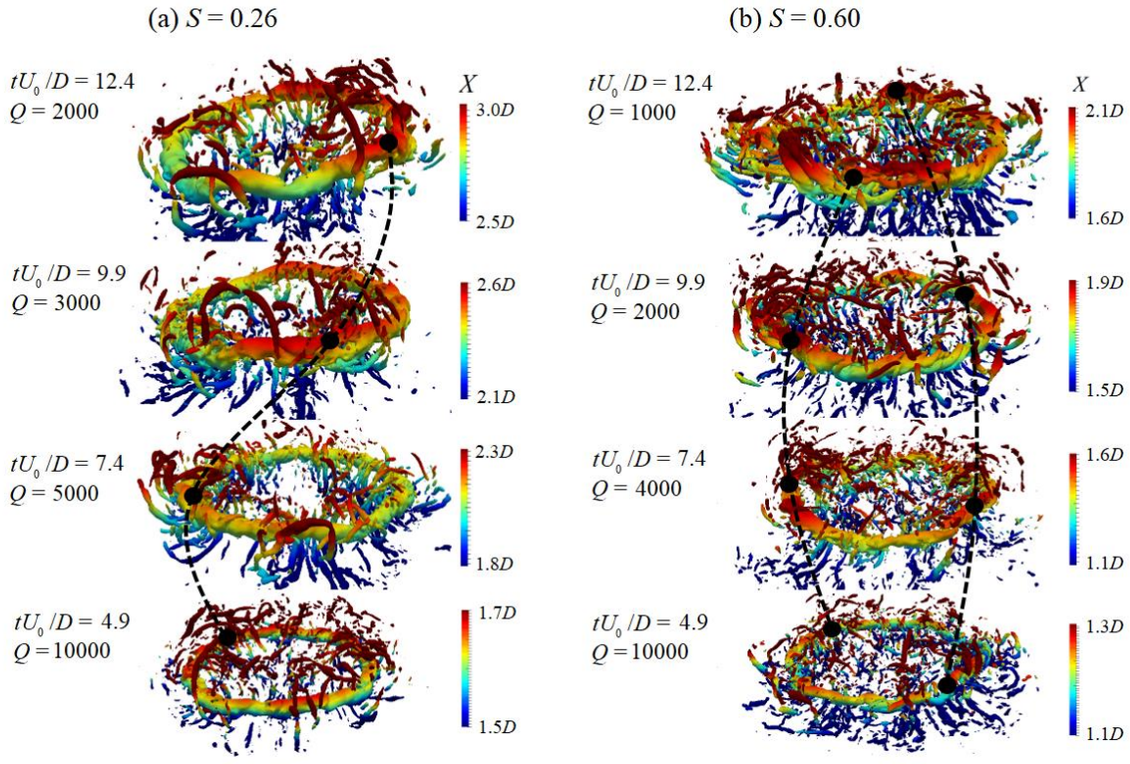

Figure 16 $m = 1$ (left) and 2 (right) modes observed in simulation results. Isosurfaces are colored by the axial coordinate value. (a) for $S = 0$ and (b) for $S = 0.60$.

5.Conclusion

The present work studies the flow dynamics of swirling vortex rings at Reynolds number $Re = 20{,}000$ using a combination of the planar- and stereo-PIV measurements and the dynamic DDES simulation. Vortex rings are issued from a piston-nozzle arrangement with axial swirlers installed at the nozzle exit. The swirl number generated ranges from $S = 0$ to 1.10. The stroke ratio $L/D = 1.5$ is employed to produce compact structures without trailing jet according to our previous study.

The simulation results agree well with the planar-PIV measurements in terms of the trajectories of the vortex ring core and the radial velocity distributions through it. According to the simulation results, the majority of the fluid in the stroke is issued to swirl at the designed swirl number. As visualized in the simulation, three types of secondary vortical structures co-exist in addition to the primary vortex ring, namely the starting wake vortices, the vane boundary vortices and the inner boundary vortices. These vortical structures, together with the swirl effects, promote the breaking down process of the primary vortex ring.

Two distinct dynamic effects are reflected in the planar-PIV measurements, the arrival time effect and the azimuthal wave effect. They cause the appeared parallel shift of the vortex ring core and tilt in radial orientation. The arrival time effect is important only for $S = 0$ and 0.26, whilst the azimuthal wave effect strengthens with the increasing swirl number. These azimuthal modes are identified using the stereo-PIV results by applying FFT in the azimuthal direction, followed by POD in the radial direction and time. It is found that for $S < 0.26$, the $m = 1$ mode had the highest energy at large formation time before which the $m = 0$ mode dominates. The $m = 2$ mode emerges at moderate formation time while the $m = 1$ mode still dominates at large formation time for $S \geq 0.41$ cases. However, energy of the $m = 1$ mode decays with increasing swirl number. Rings with $S = 1.10$ show comparable energy content in mode $m = 0$, 1 and 2 at large time. The $m = 1$ and 2 modes can also be clearly identified in simulations. The $m = 2$ mode shows large

spiral pitch growing with formation time, which echoes the existence of large-amplitude azimuthal mode along the vortex ring core.

Acknowledgements

The authors gratefully acknowledge financial support for this study from the Engineering and Physical Sciences Research Council of the UK (EP/P004377/1).

References

1. C. L. Gargan-Shingles, M. Rudman, and K. Ryan, "The evolution of swirling axisymmetric vortex rings," Physics of Fluids **27**, 087101 (2015).

2. M. Cheng, J. Lou, and T. T. Lim, "Vortex ring with swirl: a numerical study," Physics of Fluids **22**, 15 (2010).

3. T. Naitoh, N. Okura, T. Gotoh, and Y. Kato, "On the evolution of vortex rings with swirl," Physics of Fluids **26**, 067101 (2014).

4. C. He, L. Gan, and Y. Liu, "The formation and evolution of turbulent swirling vortex rings generated by axial swirlers," Flow, Turbulence and Combustion 1 (2019).

5. M. Gharib, E. Rambod, and K. Shariff, "A universal time scale for vortex ring formation," Journal of Fluid Mechanics **360**, 121 (1998).

6. M. Rosenfeld, E. Rambod, and M. Gharib, "Circulation and formation number of laminar vortex rings," Journal of Fluid Mechanics **376**, 297 (1998).

7. L. Gan, "An experimental study of turbulent vortex rings using particle image velocimetry," University of Cambridge, 2010.

8. S. Candel, D. Durox, T. Schuller, J.-F. Bourgouin, and J. P. Moeck, "Dynamics of swirling flames," Annual review of fluid mechanics **46**, 147 (2014).

9. P. Billant, J.-M. Chomaz, and P. Huerre, "Experimental study of vortex breakdown in swirling jets," Journal of Fluid Mechanics **376**, 183 (1998).

10. S. V. Alekseenko, S. S. Abdurakipov, M. Y. Hrebtov, M. P. Tokarev, V. M. Dulin, and D. M. Markovich, "Coherent structures in the near-field of swirling turbulent jets: a tomographic PIV study," International Journal of Heat and Fluid Flow **70**, 363 (2018).

11. H. Liang, and T. Maxworthy, "An experimental investigation of swirling jets," Journal of Fluid Mechanics **525**, 115 (2005).

12. P. Meliga, F. Gallaire, and J.-M. Chomaz, "A weakly nonlinear mechanism for mode selection in swirling jets," Journal of Fluid Mechanics **699**, 216 (2012).

13. F. Gallaire, and J.-M. Chomaz, "Mode selection in swirling jet experiments: a linear stability analysis," Journal of Fluid Mechanics **494**, 223 (2003).

14. M. Vanierschot, J. S. Müller, M. Sieber, M. Percin, B. W. van Oudheusden, and K. Oberleithner, "Single-and double-helix vortex breakdown as two dominant global modes in turbulent swirling jet flow," Journal of Fluid Mechanics **883**, (2020).

15. T. Loiseleux, and J.-M. Chomaz, "Breaking of rotational symmetry in a swirling jet experiment," Physics of Fluids **15**, 511 (2003).

16. K. Oberleithner, M. Sieber, C. Nayeri, C. Paschereit, C. Petz, H.-C. Hege, B. Noack, and I. Wygnanski, "Three-dimensional coherent structures in a swirling jet undergoing vortex breakdown: stability analysis and empirical mode construction," Journal of Fluid Mechanics **679**, 383 (2011).

17. V. Stetsyuk, N. Soulopoulos, Y. Hardalupas, and A. Taylor, "Scalar dissipation rate statistics in turbulent swirling jets," Physics of Fluids **28**, 075104 (2016).

18. C. Gargan-Shingles, M. Rudman, and K. Ryan, "The linear stability of swirling vortex rings," Physics of Fluids **28**, 114106 (2016).

19. H. E. Chuangxin, Y. Liu, and S. Yavuzkurt, "A dynamic delayed detached-eddy simulation model for turbulent flows," Computers & Fluids **146**, 174 (2017).
20. Y.-H. Liao, and J. C. Hermanson, "Turbulent structure and dynamics of swirled, strongly pulsed jet diffusion flames," Combustion Science and Technology **185**, 1602 (2013).
21. K. Akselvoll, and P. Moin, "Large-eddy simulation of turbulent confined coannular jets," Journal of Fluid Mechanics **315**, 387 (1996).
22. F. R. Menter, "Improved two-equation k-omega turbulence models for aerodynamic flows," (1992).
23. M. S. Gritskevich, A. V. Garbaruk, J. Schütze, and F. R. Menter, "Development of DDES and IDDES formulations for the k-ω shear stress transport model," Flow, turbulence and combustion **88**, 431 (2012).
24. S. E. Widnall, and C.-Y. Tsai, "The instability of the thin vortex ring of constant vorticity," Philosophical Transactions of the Royal Society of London. Series A, Mathematical and Physical Sciences **287**, 273 (1977).
25. L. Ma, L. Feng, C. Pan, Q. Gao, and J. Wang, "Fourier mode decomposition of PIV data," Science China Technological Sciences **58**, 1935 (2015).
26. C. Ball, H. Fellouah, and A. Pollard, "The flow field in turbulent round free jets," Progress in Aerospace Sciences **50**, 1 (2012).
27. M. Yoda, L. Hesselink, and M. Mungal, "The evolution and nature of large‐scale structures in the turbulent jet," Physics of Fluids A: Fluid Dynamics **4**, 803 (1992).
28. J. Tso, and F. Hussain, "Organized motions in a fully developed turbulent axisymmetric jet," Journal of Fluid Mechanics **203**, 425 (1989).
29. S. Gamard, W. K. George, D. Jung, and S. Woodward, "Application of a "slice" proper orthogonal decomposition to the far field of an axisymmetric turbulent jet," Physics of Fluids **14**, 2515 (2002).
30. D. Jung, S. Gamard, and W. K. George, "Downstream evolution of the most energetic modes in a turbulent axisymmetric jet at high Reynolds number. Part 1. The near-field region," Journal of Fluid Mechanics **514**, 173 (2004).

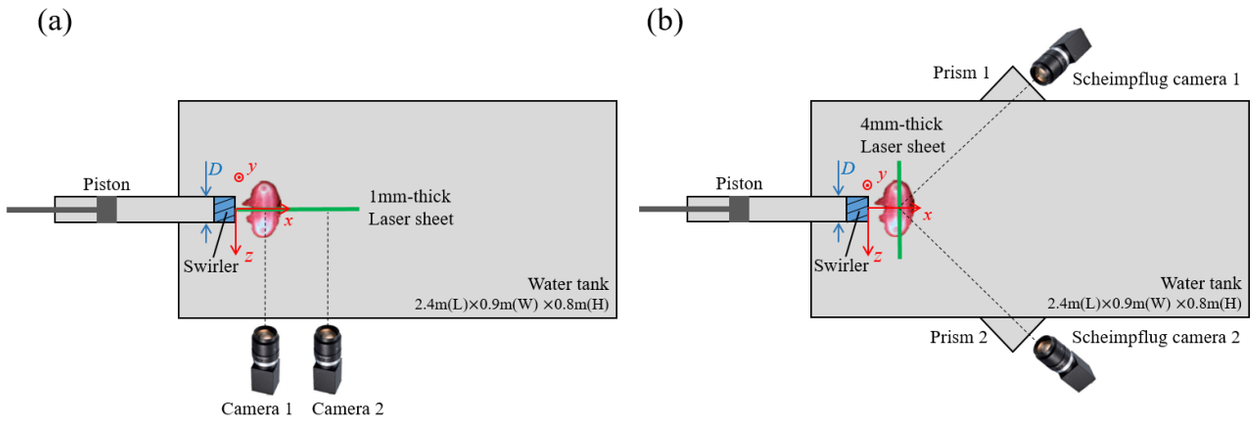

Figure 1 The schematic diagram (top view) of (a) the planar-PIV and (b) stereo-PIV measurements.

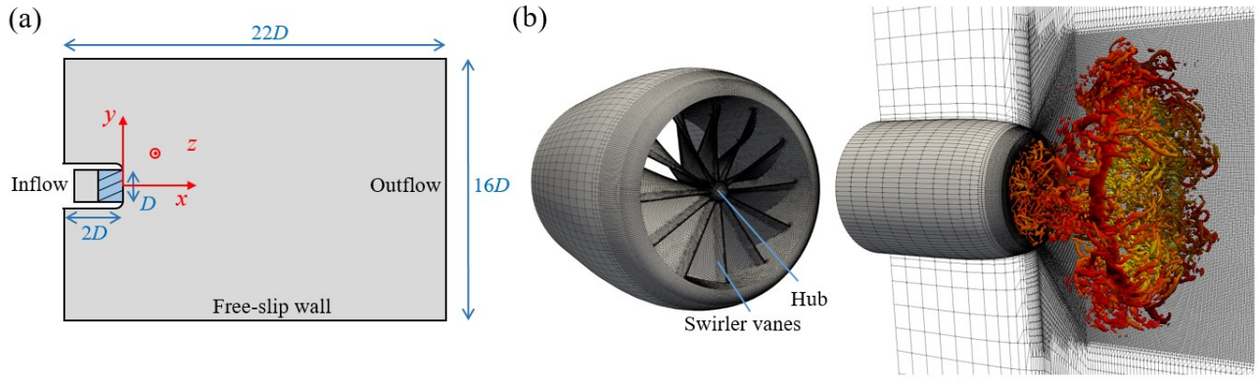

Figure 2 (a) The schematic diagram of the numerical setups (side view) and (b) the nozzle geometry with $\beta = 40^o$ and computational grid (isosuface shows the ring structure at $tU_0/D = 5$).

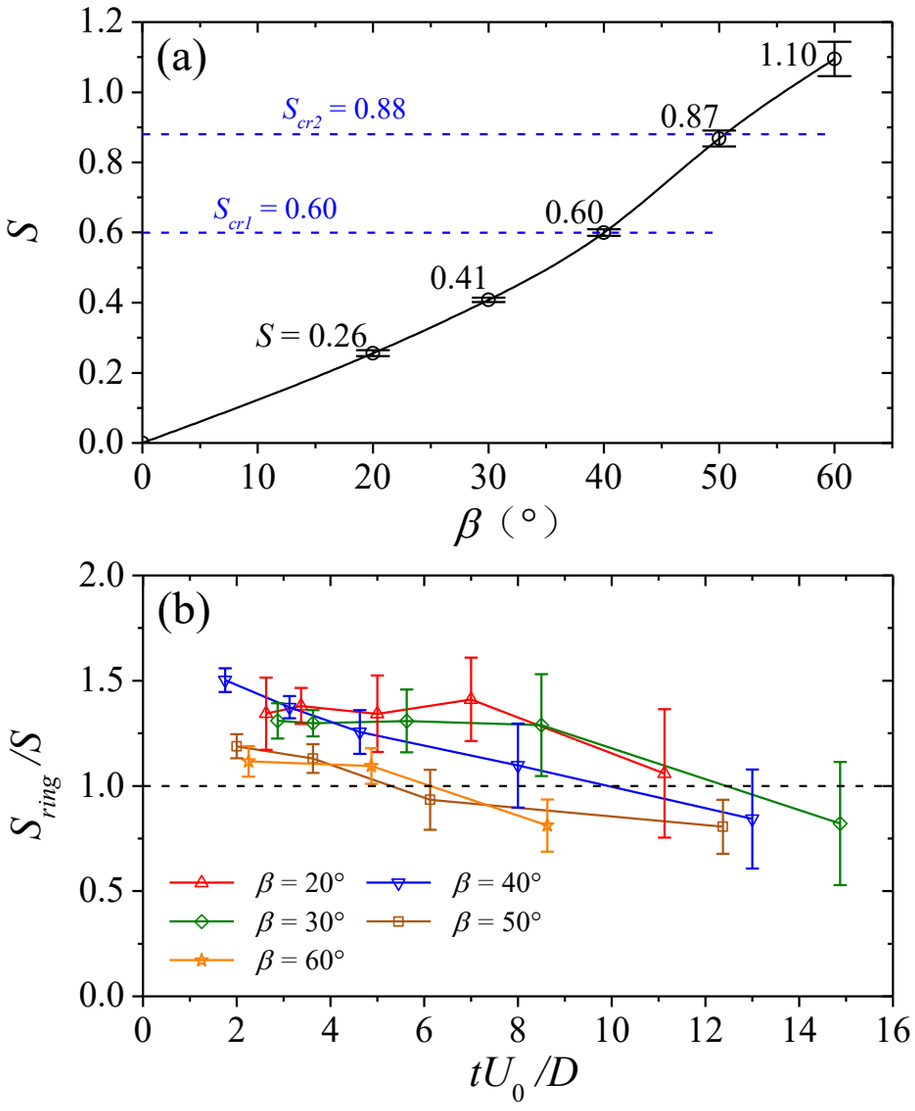

Figure 3 Fully developed swirl numbers of each swirler geometry measured by planar-PIV at the steady state jet condition (a) and the dependence of the maximum sectional swirl numbers of the flow on the formation time measured by stereo-PIV (b). Error bars are determined using 100 repeated flow realizations.

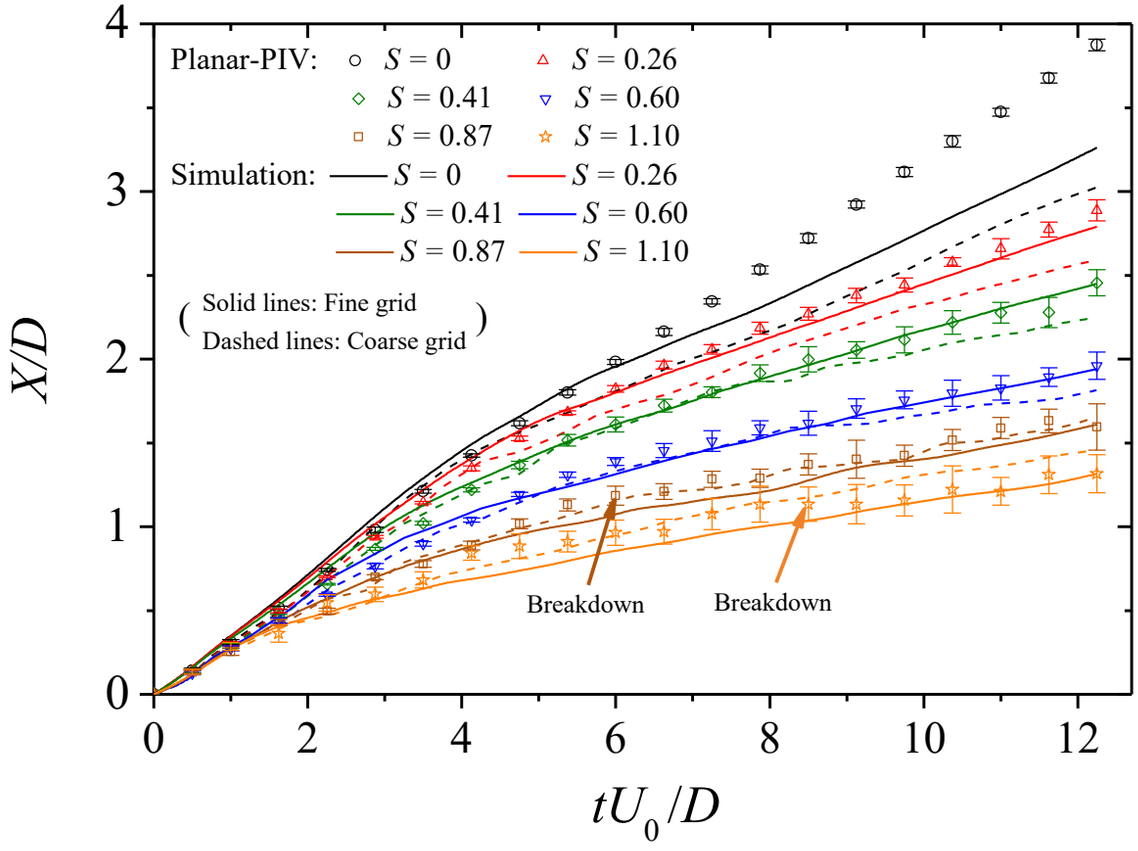

Figure 4 Axial trajectories of the vortex ring core: comparison of the present dynamic DDES results with the planar-PIV measurements. Error bars are determined using 20 repeated flow realizations. (Fine grid: 2 levels of refinement; Coarse grid: 1 level of refinement)

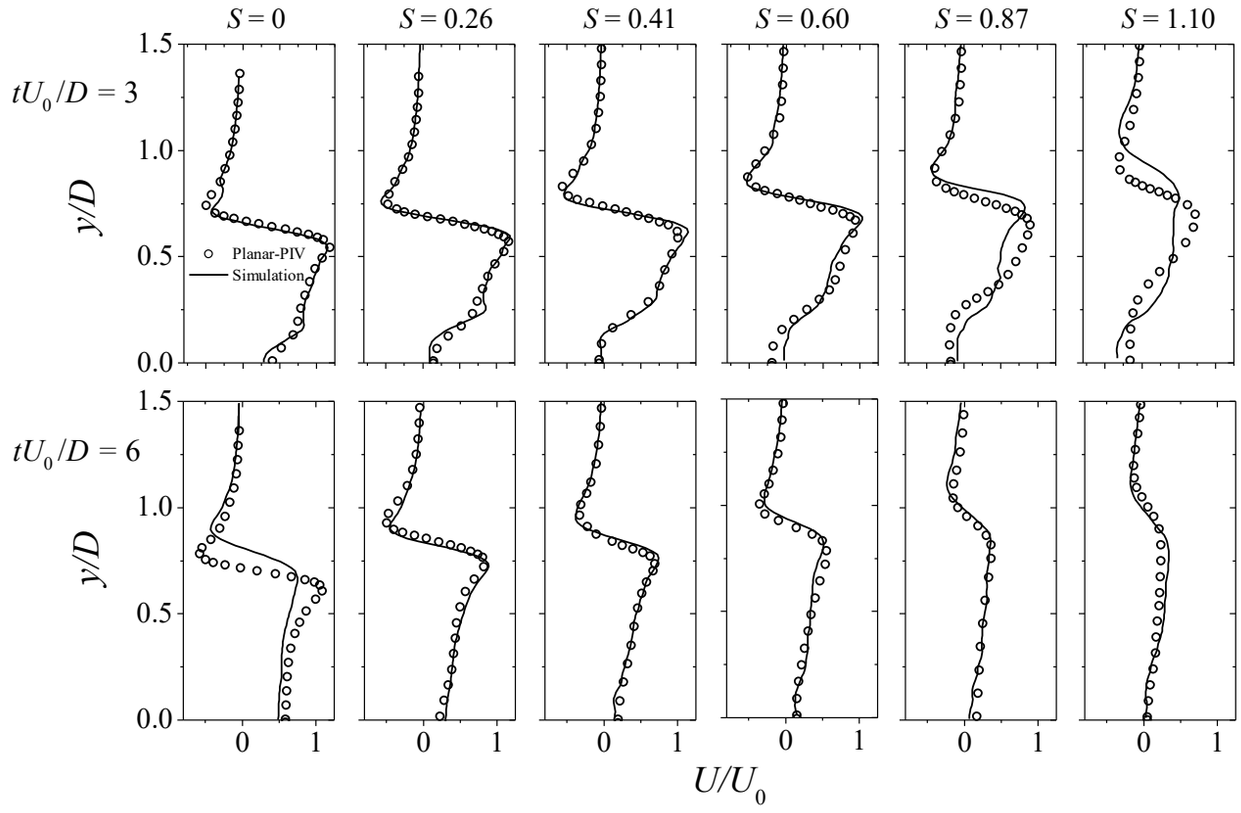

Figure 5 Comparison of axial velocity distributions of dynamic DDES and planar-PIV results at $tU_0/D = 3$ (upper row) and 6 (lower row).

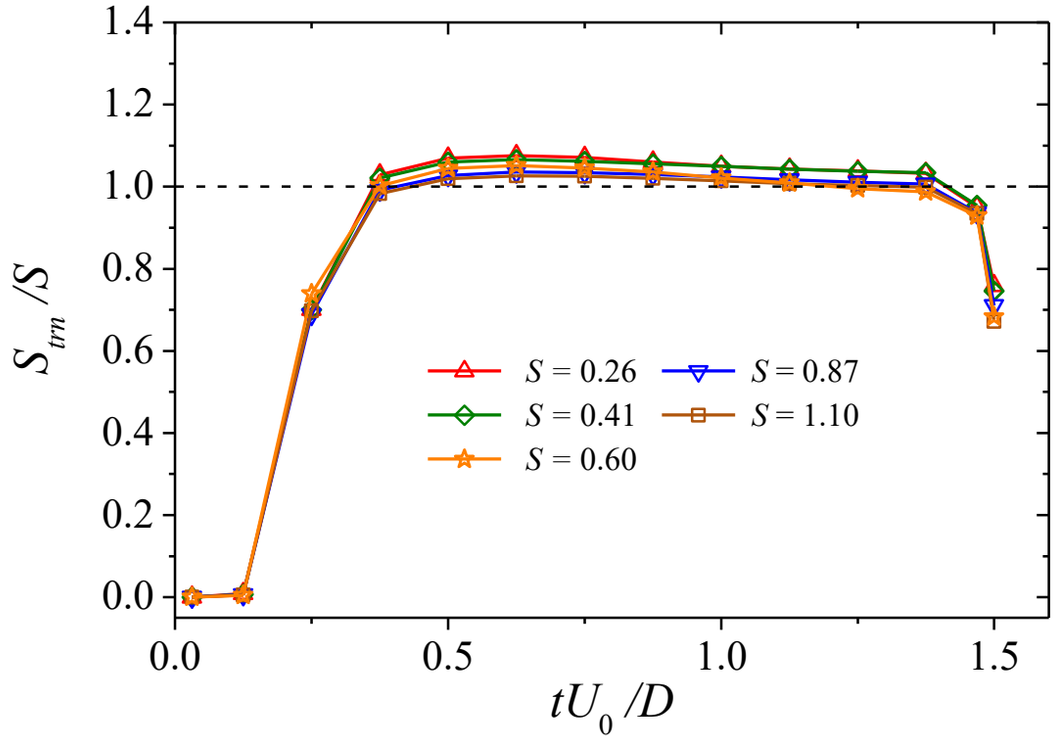

Figure 6 The transient swirl number at the swirler exit calculated using the simulation results.

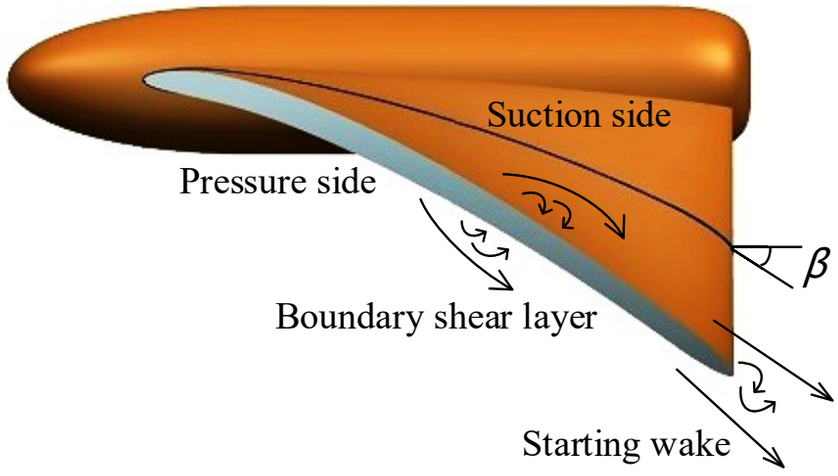

Figure 7 Schematic diagram of the starting wake and vane boundary vortices generation

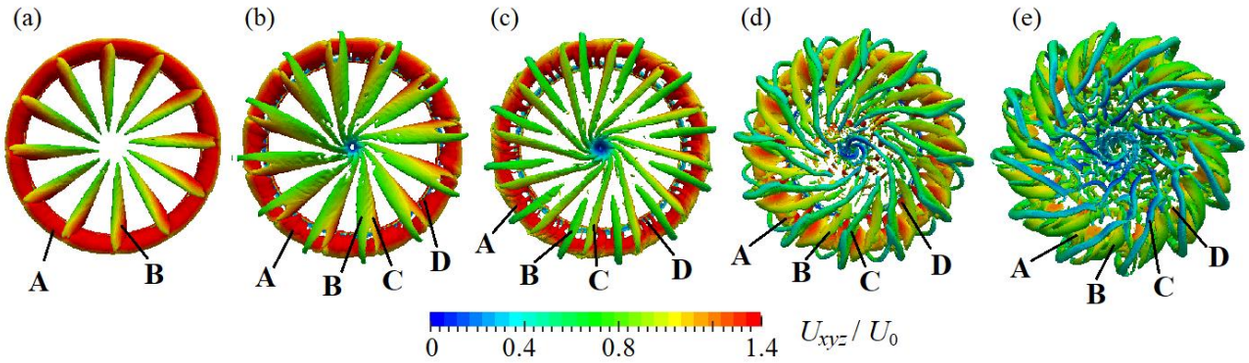

Figure 8 Three-dimensional structures of the primary vortex ring and secondary vortices for $S = 0.60$ at $tU_0/D =$ (a) 0.25, (b) 0.38, (c) 0.50, (d) 1.13 and (e) 1.50. Simulation results. $U_{xyz} = \sqrt{U_x^2 + U_y^2 + U_z^2}$ denotes the velocity amplitude in three-dimensional domain. Different vortical structures are named by: **A** primary vortex ring, **B** starting wake vortices, **C** vane boundary vortices and **D** inner boundary vortices.

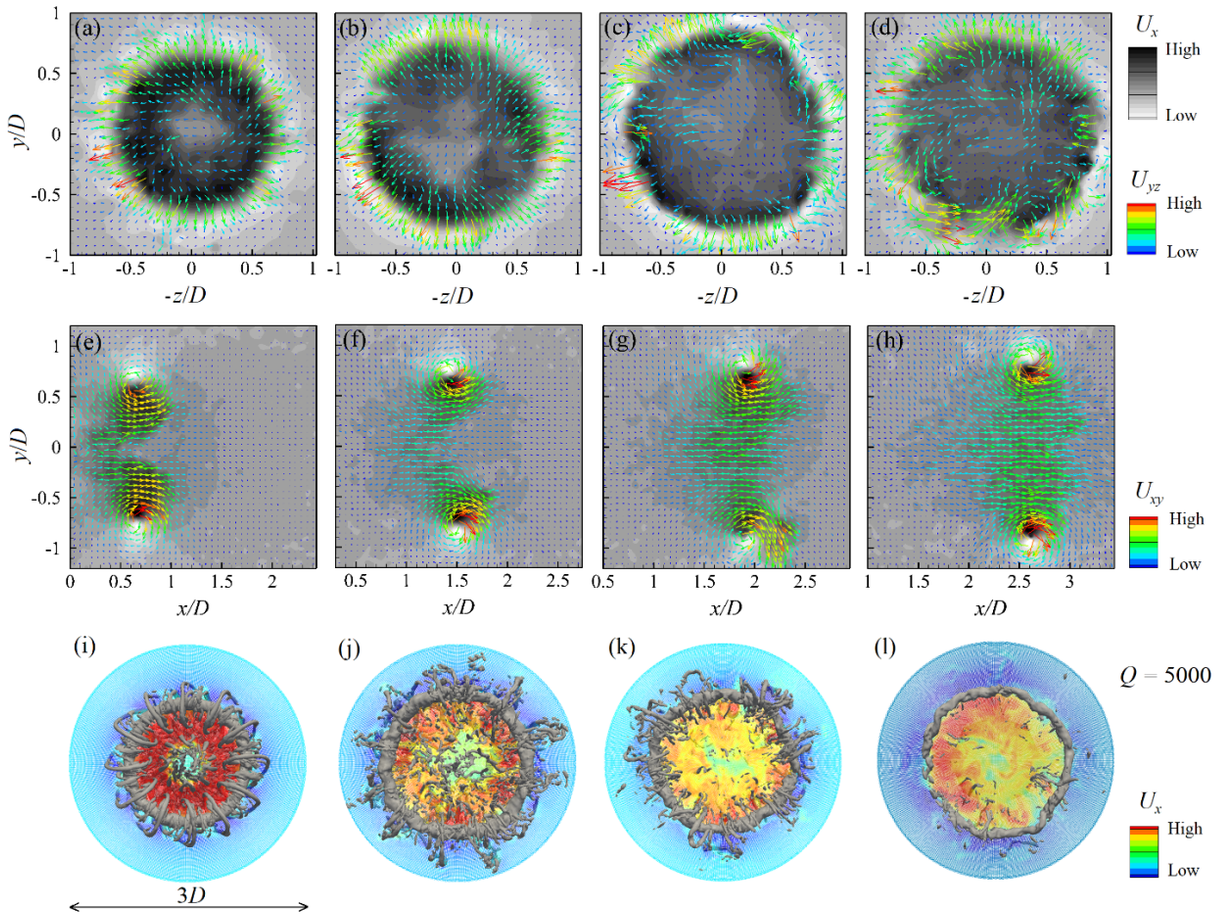

Figure 9 Instantaneous fields of the vortex ring of $S = 0.26$ at different formation time obtained by stereo-PIV (a~d), planar-PIV (e~h) and simulation (i~l). U_{xy} and U_{yz} denote the velocity amplitude in $x-y$ and $y-z$ planes.

(a) $tU_0/D = 2.6$, (b) $tU_0/D = 5.0$, (c) $tU_0/D = 7.0$, (d) $tU_0/D = 11.1$,
(e) $tU_0/D = 2.4$, (f) $tU_0/D = 4.9$, (g) $tU_0/D = 6.8$, (h) $tU_0/D = 11.1$,
(i) $tU_0/D = 2.6$, (j) $tU_0/D = 5.0$, (k) $tU_0/D = 7.0$, (l) $tU_0/D = 11.1$.

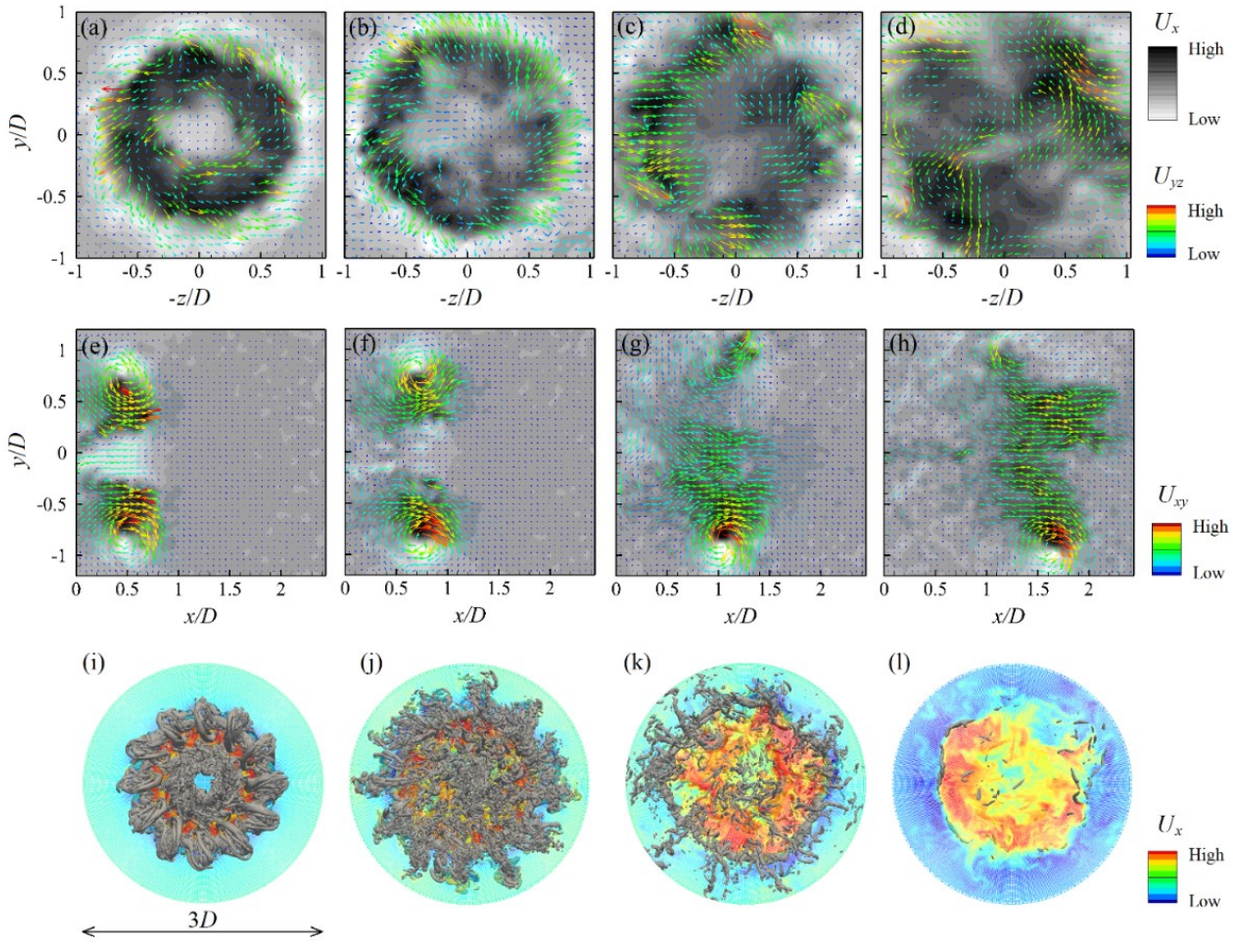

Figure 10 Instantaneous fields of the vortex ring of $S = 0.87$ at different formation time obtained by stereo-PIV (a~d), planar-PIV (e~h) and simulation (i~l). U_{xy} and U_{yz} denote the velocity amplitude in $x-y$ and $y-z$ planes.

(a) $tU_0/D = 2.0$, (b) $tU_0/D = 3.6$, (c) $tU_0/D = 6.1$, (d) $tU_0/D = 12.4$,
(e) $tU_0/D = 2.4$, (f) $tU_0/D = 3.6$, (g) $tU_0/D = 6.1$, (h) $tU_0/D = 12.4$,
(i) $tU_0/D = 2.0$, (j) $tU_0/D = 3.6$, (k) $tU_0/D = 6.1$, (l) $tU_0/D = 12.4$.

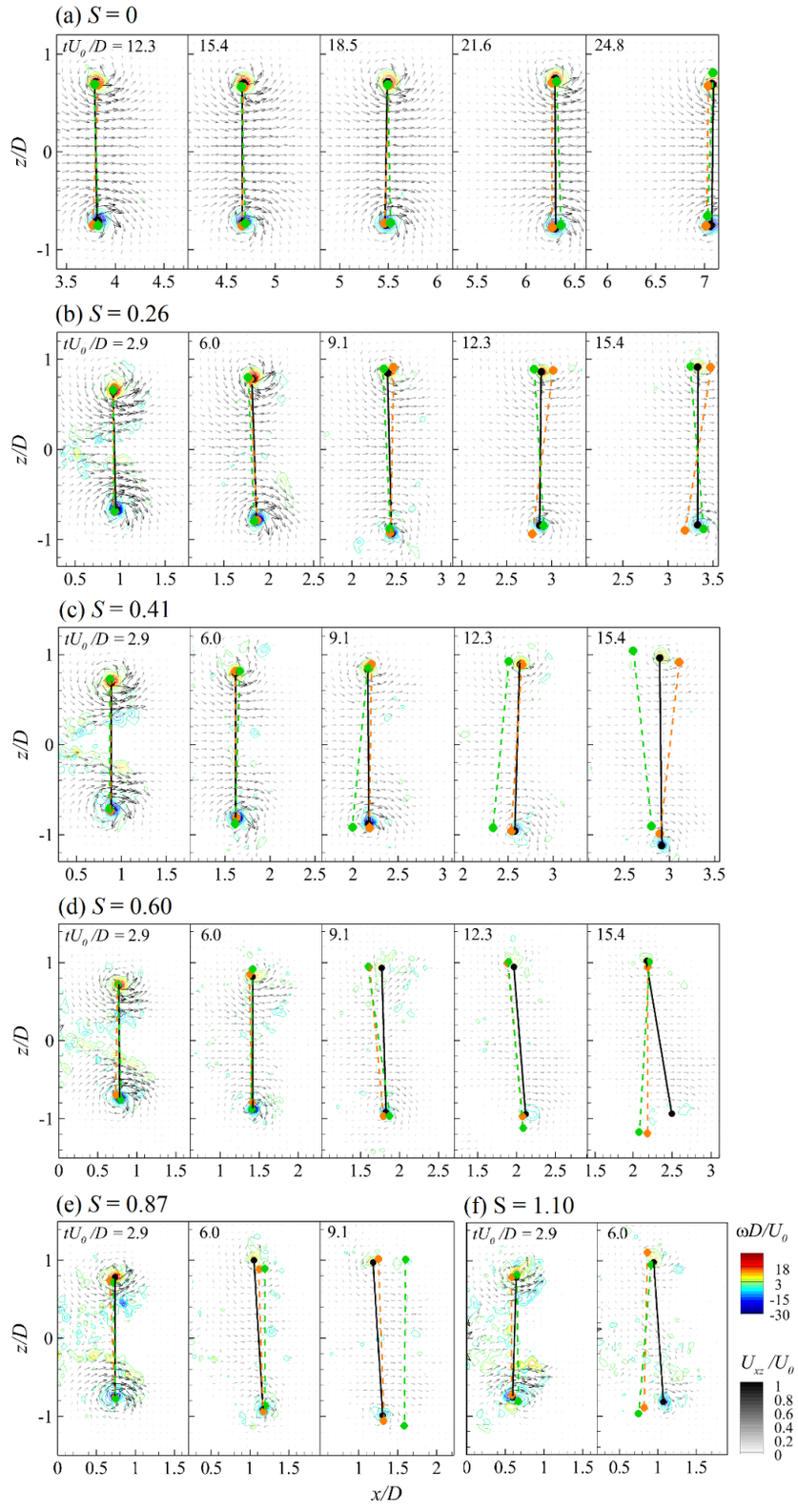

Figure 11 Instantaneous ring core location for three independent realizations (denoted by black, green and orange dots and bars) determined by planar-PIV. (a-f) for $S =$ 0, 0.26, 0.41, 0.60, 0.87 and 1.10 respectively.

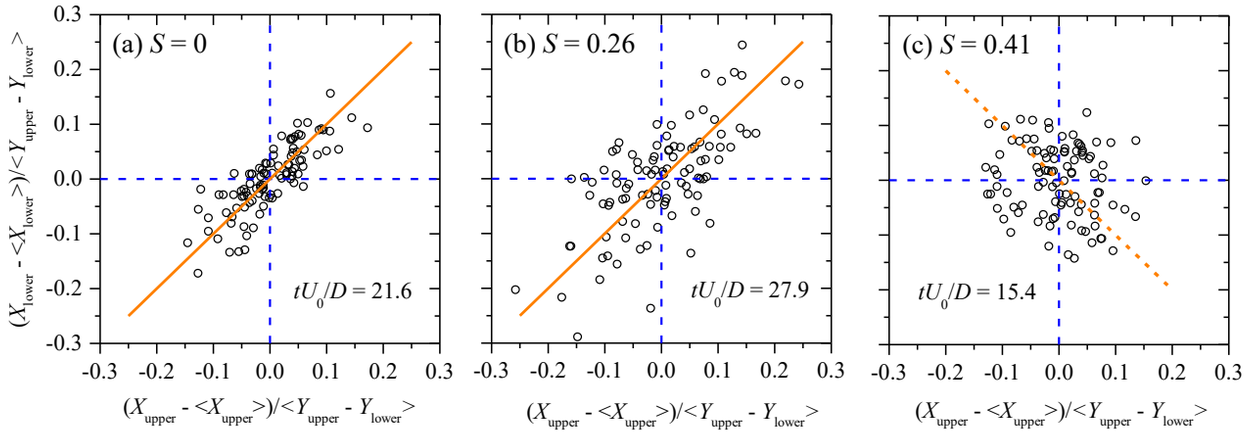

Figure 12 Coordinate maps of the upper and lower parts of the ring cores measured by planar-PIV. Each data point represents a realization. (a-c) for $S = 0$, 0.26 and 0.41 respectively.

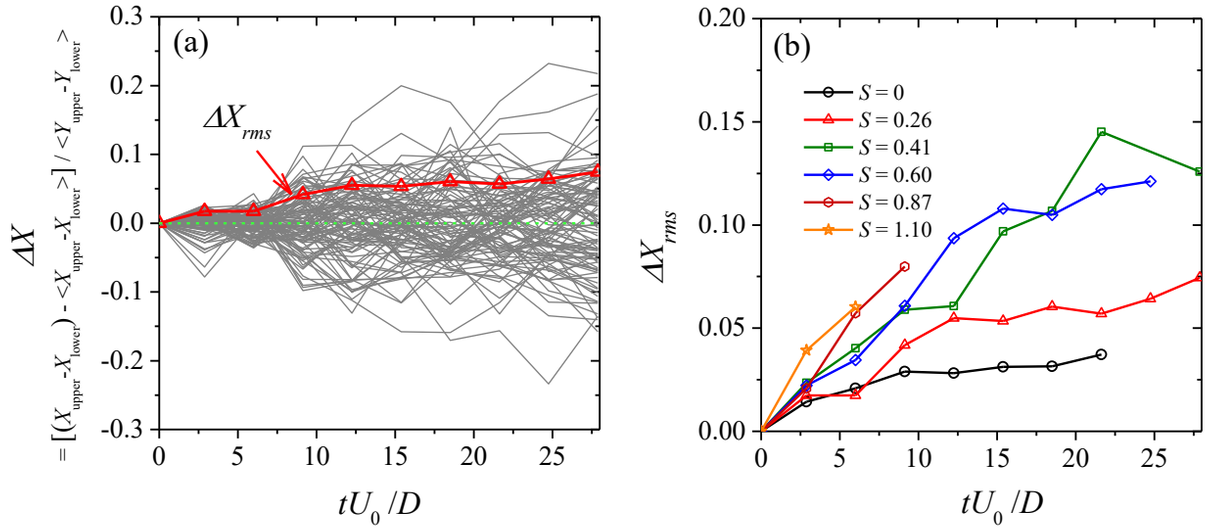

Figure 13 Variation of the axial distances between the upper and lower core measured by planar-PIV. 100 realizations and the corresponding root-mean-squares of $S = 0.26$ are plotted in (a), the variation of the root-mean-squares for different S is plotted in (b).

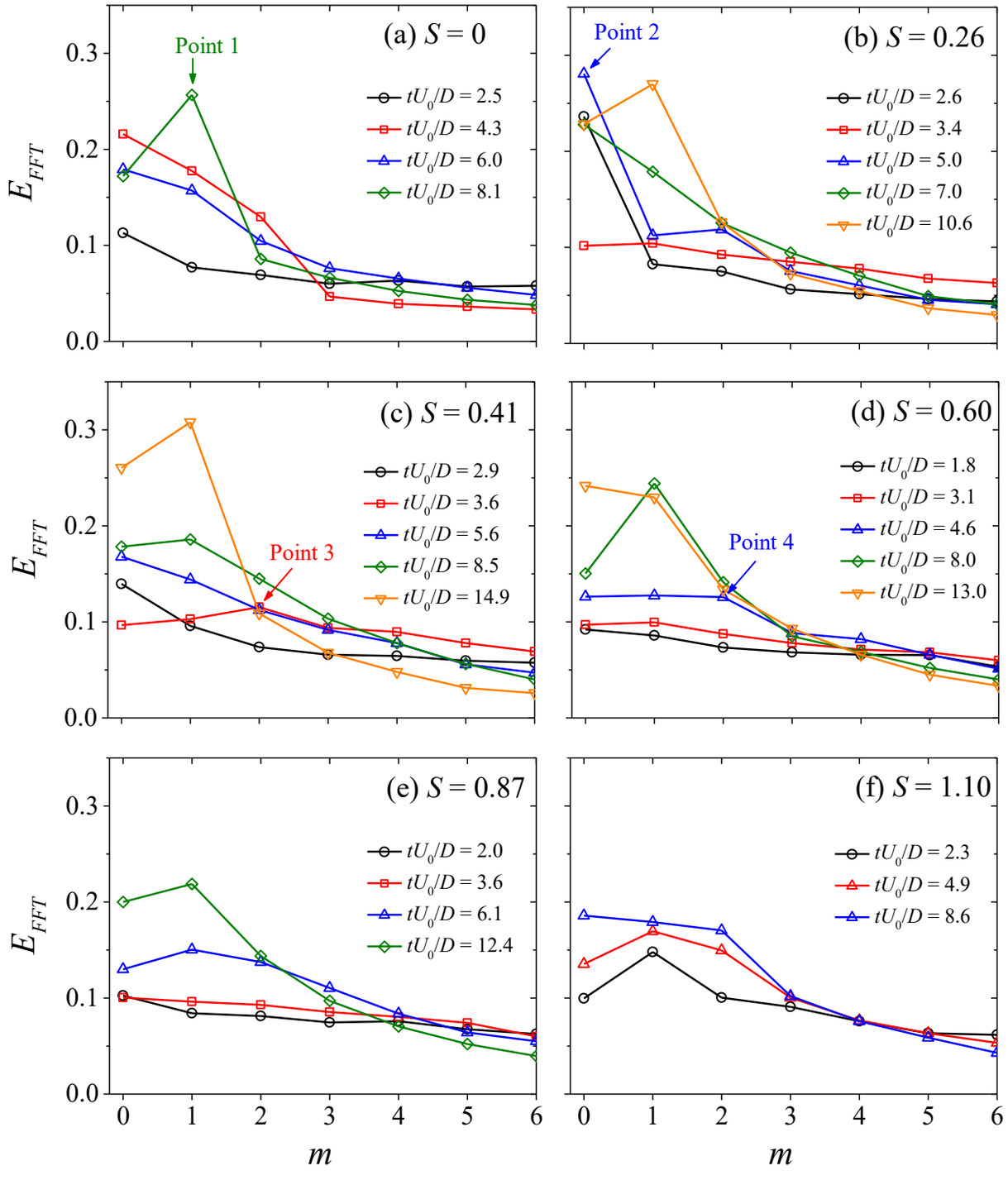

Figure 14 Energy of the Fourier modes at each azimuthal wavenumber calculated using stereo-PIV results. (a-f) for $S =$ 0, 0.26, 0.41, 0.60, 0.87 and 1.10 respectively.

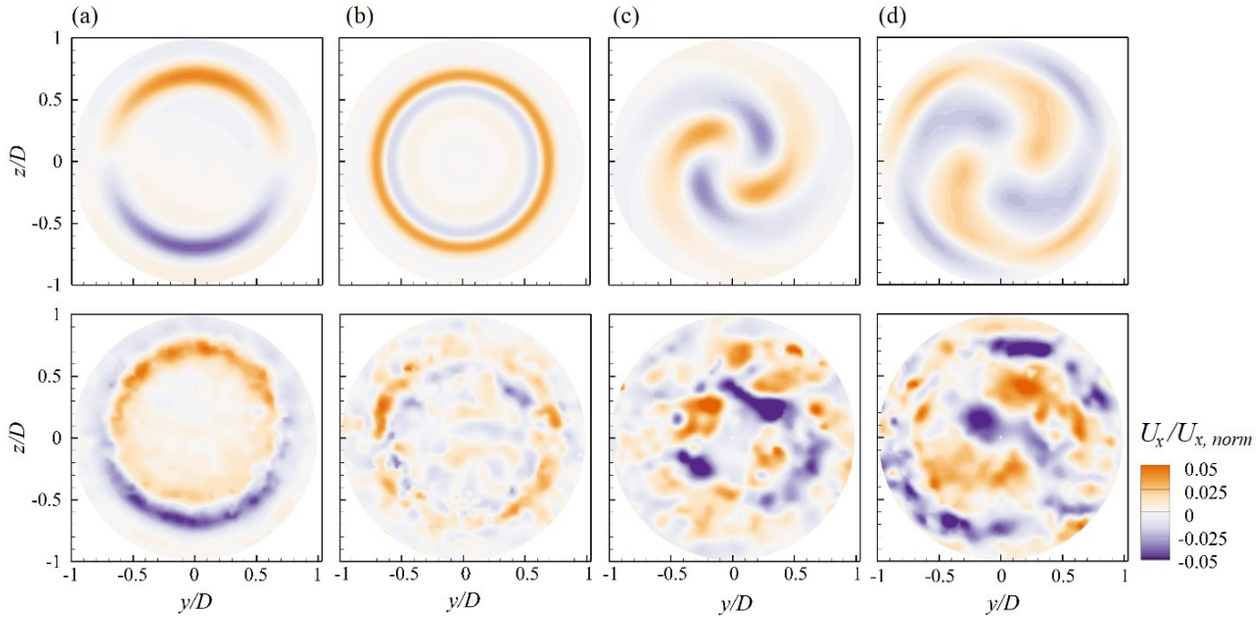

Figure 15 Azimuthal modes (upper) captured using stereo-PIV measurements and the instantaneous fluctuating axial velocity (lower) at the points marked in Figure 13. Point 1 (a), Point 2 (b), Point 3 (c) and Point 4 (d). velocity is normalized by the matrix norm $U_{x,norm}$.

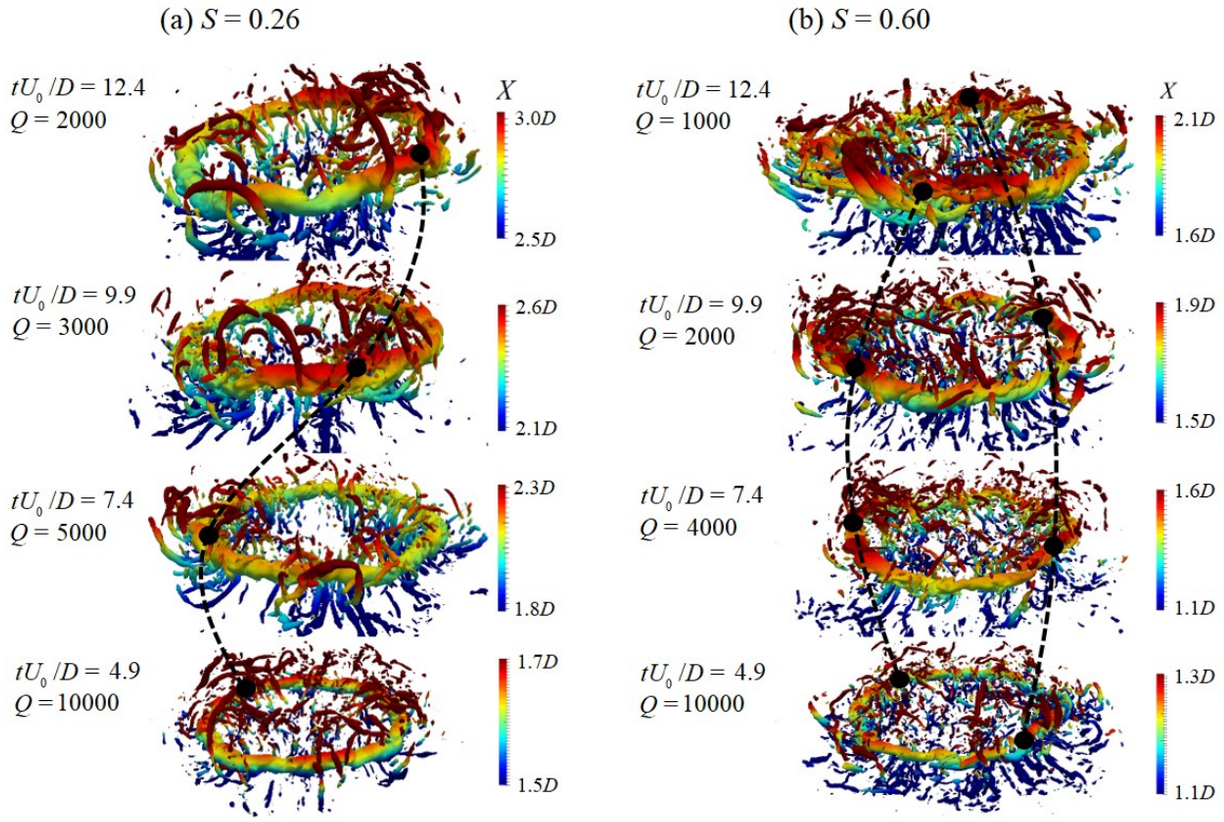

Figure 16 $m = 1$ (left) and 2 (right) modes observed in simulation results. Isosurfaces are colored by the axial coordinate value. (a) for $S = 0$ and (b) for $S = 0.60$.